2008

Nanostructured transition metal oxide materials for supercapacitor application

Bei Wang
University of Wollongong

Nanostructured Transition Metal Oxide Materials for Supercapacitor Application

A thesis submitted in fulfillment of the

requirements for the award of the degree

Master of Engineering – Research

Bei Wang, B.Sc.

University of Wollongong

Institute for Superconducting and Electronic Materials

Faculty of Engineering

2008

ACKNOWLEDGEMENTS

Firstly, I would express my deep gratitude to my supervisors, Assoc. Prof. Guoxiu Wang and Dr. Konstantin Konstantinov, for their consistent supervision, guidance, and arrangements to facilitate my studies throughout the whole period of my research work.

All the staff and research students in the ISEM and the Faculty of Engineering deserve real gratitude for their assistance in the interpreting instructions for devices, setting up facilities, and providing explanations of basic knowledge, as well as for help in interpreting and processing the experimental data, and in dealing with all the various administrative issues.

Special thanks are due to the members of our research group, as they provided generous and effective co-operation and shared their priceless research experiences with me. I am also grateful that Dr. David Wexler performed excellent TEM measurements and analysis for me, while Dr. Tania Silver revised all my papers and made a great contribution to the editing of this thesis.

Finally, I appreciate the endless support and encouragement from my dear parents in China. Without their eternal love, I would not have overcome all the difficulties in my daily life and completed the entire research program.

ABSTRACT

Supercapacitors are new generation energy storage devices, which can provide higher energy density (compared with conventional capacitors) and higher power density (compared with batteries). Amorphous ruthenium oxide, applied as an electrode material, yields the best specific capacitance value of 720 F g^{-1} [1]. However, the high cost of ruthenium oxide limits its extensive use in supercapacitors. Alternative materials, such as activated carbon, transition metal oxides, and conducting polymers, are being comprehensively studied. In this thesis, the transition metal oxides, V_2O_5/carbon composite, Co_3O_4, and Fe_2O_3, were intensively investigated as supercapacitor electrode candidates. Several techniques, X-ray diffraction, scanning and transmission electron microscopy, Brunauer-Emmett-Teller techniques, and thermogravimetric analysis, were applied to characterize the as-prepared materials, while the electrochemical properties were examined by the cyclic voltammetry. The maximum specific capacitance was 295 F g^{-1}, 281 F g^{-1}, 72 F g^{-1} for V_2O_5/carbon nanocomposite, Co_3O_4 nanorods, and Fe_2O_3 nanorods, respectively, in various electrolytes at a voltage scan rate of 5 mV s^{-1}. The morphology and large specific surface area of the nanomaterials, as well as the presence of pores in the nanostructure, are thought to contribute to the excellent electrochemical performance.

CONTENTS

Chapter 1. Introduction

Supercapacitors, also called chemical capacitors, ultracapacitors, or hybrid capacitors, are electrochemical capacitors that have unusually high energy densities compared to common capacitors. The supercapacitor is much like a regular capacitor except that it provides very high capacitance in a small package. Energy storage is by means of static charge rather than by an electro-chemical process that is inherent to the battery. The supercapacitor can be charged by applying a voltage differential between the positive and negative plates [2]. Whereas a regular capacitor consists of conductive foils and a dry separator, the supercapacitor uses special electrodes along with an electrolyte.

The supercapacitor operating principle is based on the double layer at the interface between the electrode (activated carbon, etc.) and the electrolyte when a voltage is applied to the terminals. The energy storage for double-layer type capacitors is primarily electrostatic, not a faradaic process as the case for batteries, but likely includes a so-called pseudocapacitive ingredient to contribute to the total capacitance [3].

As such supercapacitors have a unique energy storage principle, very high rates of charge and discharge, little degradation over hundreds of thousands of cycles, good reversibility, constituent materials with low toxicity, and high cycling efficiency (95% or more), more and more papers are published every year, focusing on this new-generation energy storage device. Many researchers have found that the performance of supercapacitors can

be significantly improved by using nanomaterials. The energy storage capability of a capacitor is directly proportional to its capacitance, which in turn is proportional to the area of the plates or electrodes. Likewise the current carrying capability is directly proportional to the area of the electrodes [4]. Therefore, in this case, there are three types of electrode materials with microstructures suitable for supercapacitors. They are: high surface area activated carbons, metal oxides, and conducting polymers. By applying such materials as electrodes, the effective area of the electrodes can be dramatically increased; hence, the capability of the supercapacitors will be enhanced.

Transition metal oxides often show high electrochemical activity and good discharge performance on the nanoscale, due to their high specific surface areas, so they are widely considered as possible electrode materials for electrochemical capacitors. So far, the best specific capacitance value is 720 F g^{-1}, which was obtained by applying amorphous ruthenium oxide as an electrode material, using a 2-mV s^{-1} scan rate in H_2SO_4 electrolyte [1]. However, the high cost of ruthenium oxide remains an obstacle to making the electrochemical capacitor technology commercially viable. Many transition metal oxides, such as oxides of manganese [5, 6], nickel [7], and cobalt [8, 9], have been evaluated and investigated for their capabilities and possibilities as alternative materials for electrochemical capacitors. The development of high energy density capacitors, electrochemical capacitors, is currently an important topic in international research.

In the work reported here, V_2O_5/carbon nanocomposites, Co_3O_4 nanorods, and Fe_2O_3

nanorods, have all been systematically studied. The synthesis methods via different routes, the characterizations of their physical properties, and their electrochemical performance as supercapacitor electrode active materials are detailed.

Chapter 2 reviews the history and development of supercapacitor technology. The principles of the energy storage mechanisms are explained though double-layer capacitance, pseudocapacitance, and hybrid supercapacitors. The three main categories of the electrode materials, activated carbon, transition metal oxides, and conducting polymers, are introduced, and their current research status is briefly discussed.

Chapter 3 introduces the experimental details that are relevant to the entire research project, including the materials and chemicals used in synthesis and electrochemical testing, and the various characterization techniques. A brief description explaining the operating principle of each facility is also given in this chapter.

Chapter 4 deals with the preparation by the spray pyrolysis technique of nanostructured vanadium pentoxide/carbon (V_2O_5/carbon) composite powders with enhanced specific capacitance. Scanning Electron Microscopy (SEM), Transmission Electron Microscopy (TEM) and high resolution TEM (HRTEM) imaging revealed a specific morphology of spherical shell agglomerates of V_2O_5 nanorods and nanoribbons, with each shell consisting of a network of one and two dimensional nanoparticles in an amorphous carbon matrix. Composite powders obtained at an optimum temperature of 450 °C

yielded a maximum specific capacitance of 295 F g^{-1} in 2 M KCl electrolyte at a 5-mV s^{-1} scan rate. The enhancement of the specific capacitance in V_2O_5/carbon composite is attributed to the distribution of amorphous carbon throughout the V_2O_5 and the particular open nanostructure.

In Chapter 5, the synthesis of one-dimensional Co_3O_4 nanorods through a hydrothermal method with a further calcination process is described. The morphology of the product is revealed to be flowerlike, with highly ordered nanoscale rods extending from the "root". The rods were formed from nanocrystalline Co_3O_4, with an average rod diameter of 150 nm. The Co_3O_4 nanorods exhibited a maximum specific capacitance of 281 F g^{-1} in 2 M KOH solution at a 5-mV s^{-1} scan rate, showing 83.4% retained specific capacitance after 1000 charge-discharge cycles.

Chapter 6 focuses on α-Fe_2O_3 nanorods, synthesized by a facile chemical route through a hydrothermal approach. Hematite Fe_2O_3 phase is present, in the form of nanocrystalline Fe_2O_3 fine rods that are joined together, with an average particle size of less than 100 nm. These rods grew in pairs with a pore in the middle, with the average rod diameter in the range of 20–60 nm. The highest specific capacitance of 72 F g^{-1} was obtained in 2 M $Na_2S_2O_3$ solution at a 5-mV s^{-1} scan rate.

Chapter 7 presents several attempts involving other transition metal oxides, examining their electrochemical properties as supercapacitor electrode materials. V_2O_5 synthesized

by precipitation and further calcinations is also reported for comparison.

A general summary is given in Chapter 8, containing an overview of the examination of selected candidate materials in this thesis, the current state of supercapacitor development, and the current challenges in this field.

Chapter 2. Literature Review

In 1957, the first supercapacitor was developed by General Electric. Applying a double-layer mechanism, it was considered that this supercapacitor stored energy in the carbon pores and showed exceptionally high capacitance [10]. In 1966, the Standard Oil Company, Cleveland (SOHIO) invented the first supercapacitor device which stored energy at a double-layer interface [11]. From then on, the development of supercapacitors proceeded very quickly, and they are of particular interest in automotive applications for hybrid vehicles and as supplementary energy storage for battery electric devices.

2.1 Introduction

Electrical energy storage is applied in various telecommunication devices, such as mobile phones and pagers, stand-by power systems, and hybrid electric vehicles. To meet all the requirements for these energy storage devices, the particular devices need to have advantages in terms of both the amount of energy stored and the maximum power. Weight, initial cost, and lifetime are also important issues. For the more demanding power requirements, people separate the energy and power requirements by providing for the peak power by using a capacitor as a pulsed power device. The capacitor is charged periodically from primary energy storage units (batteries). Traditional capacitors are not suitable to provide pulsed power where significant energy is needed, as they provide energy in electronic circuits so that enough energy cannot be stored in the volume and

weight available. Therefore, the development of high energy density capacitors (supercapacitors or electrochemical capacitors) has been undertaken by various groups all over the world.

In Fig. 2-1, the roles of different energy storage devices with diverse energy and power supplies are illustrated [12]. Among all the energy storage devices, batteries have become the most common ones and are involved in most applications, because they can store large amounts of energy in a relatively small volume and weight, and provide suitable levels of power for many applications. However, the disadvantages lie in the shelf and cycle life with most types of batteries. Supercapacitors are being developed as an attractive alternative to pulsed batteries, as they have much higher power and much longer shelf and cycle life than batteries. It is the low energy density for supercapacitors that in most cases determines the feasibility of their use in a particular high power application.

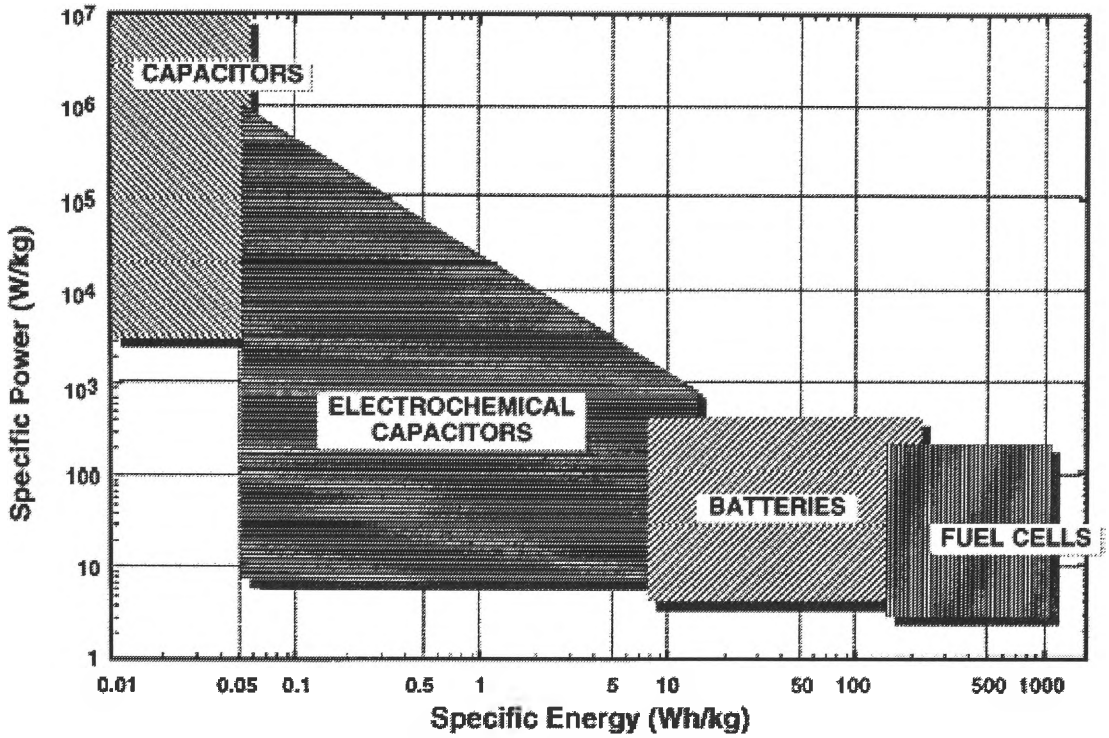

Figure 2-1. Simplified Ragone plot of the energy storage domains for the various electrochemical energy conversion systems [12].

2.2 Energy Storage Mechanisms

The most common electrical energy storage devices are batteries, fuel cells and capacitors. Capacitors store energy by charge separation, and consist of a thin layer of dielectric material and metal plates as the terminals for the devices. The expression of energy stored in a capacitor is given by

$$E = 1/2\ CV^2 \qquad (2\text{-}1),$$

where C is the capacitance (Farads) and V is the voltage between the terminal plates. The relationship between the charge, Q, stored in the capacitor (given by CV), the dielectric constant (K), which determines the capacitance of a dielectric capacitor, the thickness (d) of the dielectric material, and its geometric area (A) is given below.

$$C = KA/d \qquad (2\text{-}2)$$

Energy storage for batteries is in chemical form in the active material in the electrodes. When a load is connected across the terminals of the battery, energy is released in electrical form. This will result in electrochemical reactions of the electrode materials with the ions transferring through the electrolyte. Those ions are provided by the electrolyte in which the electrodes are immersed. Assume that the voltage of the cell is expressed as V, and the electrical charge, current-time (It), is given as Q, which is

transferred to the load during the chemical reaction, then the useable energy stored in the battery is given as VQ. Fig. 2-2 represents a battery with the key features [13]. The requirements on electron and ion conduction in the electrodes and the electrolyte are valid for all three energy storage systems.

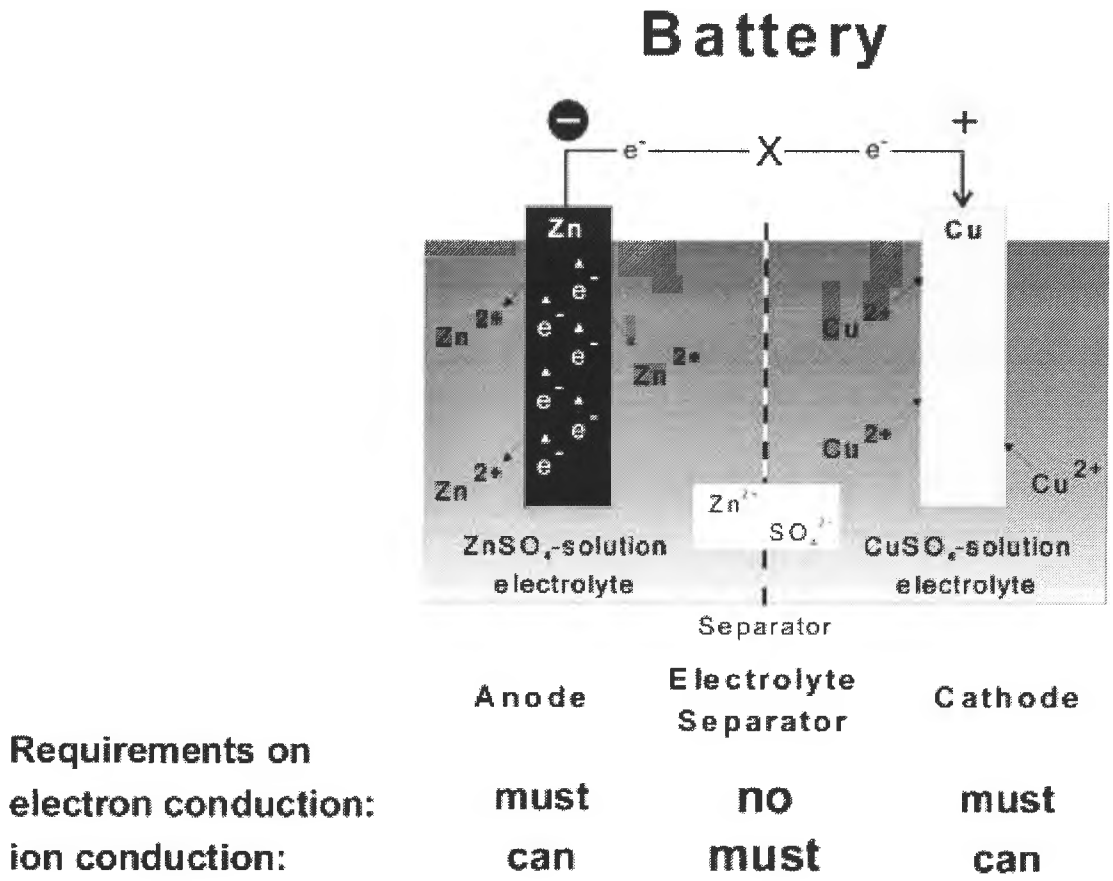

Figure 2-2. Representation of a battery, showing the key features of battery operation and the requirements on electron and ion conduction [13].

Fuel cells, the second type of energy storage devices, also convert chemical energy into electrical energy like batteries do. As in batteries and other electrochemical cells, fuel cells consist of an anode, a cathode, and an electrolyte. At the anode and the cathode, respectively, oxidation and reduction occurs, while in the electrolyte, ions carry the

current between the electrodes. The fuel and the oxidant in the fuel cells are supplied continuously from an external source, but in batteries, these components are contained within the cell compartment. As long as the fuel is supplied, fuel cells can be operated, so they are also described as internal combustion engines. Electrical recharge is not applied to fuel cells, but the tank can be refilled with fuel after use. From an operational point of view, the fuel of choice is hydrogen gas, because the exhaust gas would be water. Other possible options are hydrocarbons, but they must be converted to hydrogen for use in a fuel cell. Fuels such as CH_3OH and CH_4 may be directly converted under certain conditions. Each type of fuel cell has its own set of processes and reactions for the operation.

A supercapacitor, sometimes referred to as an electrochemical capacitor, differs from a battery, although it has two electrodes immersed in an electrolyte with a separator between the electrodes. The electrodes are fabricated from nanoscale, high surface area, porous materials. Compared to batteries, the surface areas of the electrode materials used in supercapacitors are much greater, with values up to 500–2000 $m^2\ g^{-1}$. Charge is stored in the micropores at or near the interface between the solid electrode material and the electrolyte. The charge and energy stored are expressed in the same way as cited previously for the simple dielectric capacitor. However, it is complicated to calculate the capacitance of the supercapacitor, as many complex phenomena occurring in the micropores of the electrode are involved.

Fig. 2-3 shows a supercapacitor (top), illustrating the energy storage in the electric double layers at the electrode-electrolyte interfaces, and a fuel cell (bottom) showing the continuous supply of reactants (hydrogen at the anode and oxygen at the cathode) and the redox reactions in the cell [13].

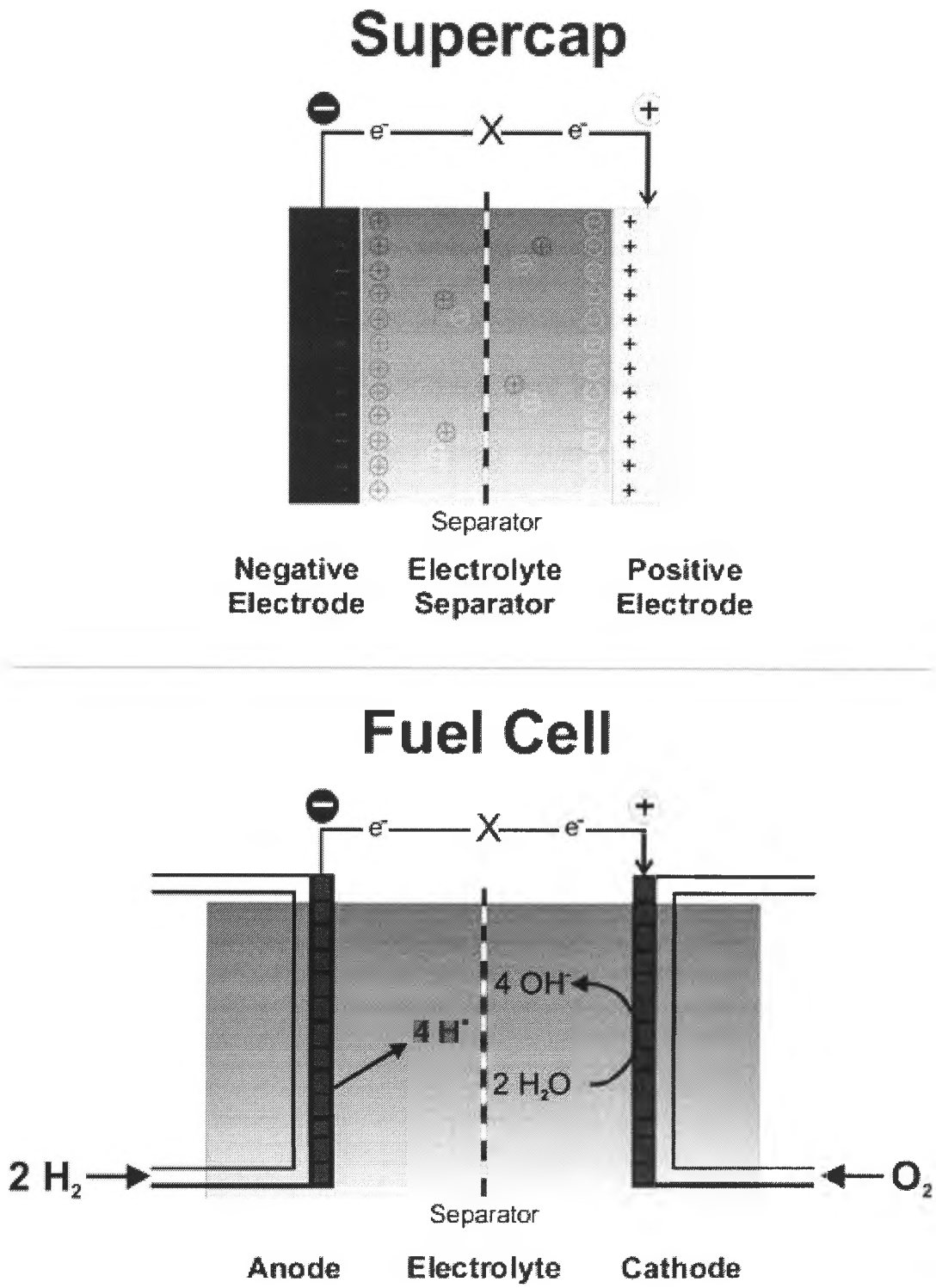

Figure 2-3. Schematic of a supercapacitor (top), and a fuel cell (bottom) [13].

2.2.1 Double-layer Capacitors

Energy is stored in the form of charge separation in double-layer capacitors. This kind of double-layer is formed at the interface between the solid electrode material surface and the liquid electrolyte in the micropores of the electrodes. A schematic of a supercapacitor is shown in Fig. 2-4 [3]. The ions are transferred between the electrodes by diffusion through the electrolyte. The energy and charge stored in the supercapacitor are $1/2\ CV^2$ and CV, respectively, as stated previously. The characteristics of the electrode material, such as surface area and pore size distribution, are related to the capacitance.

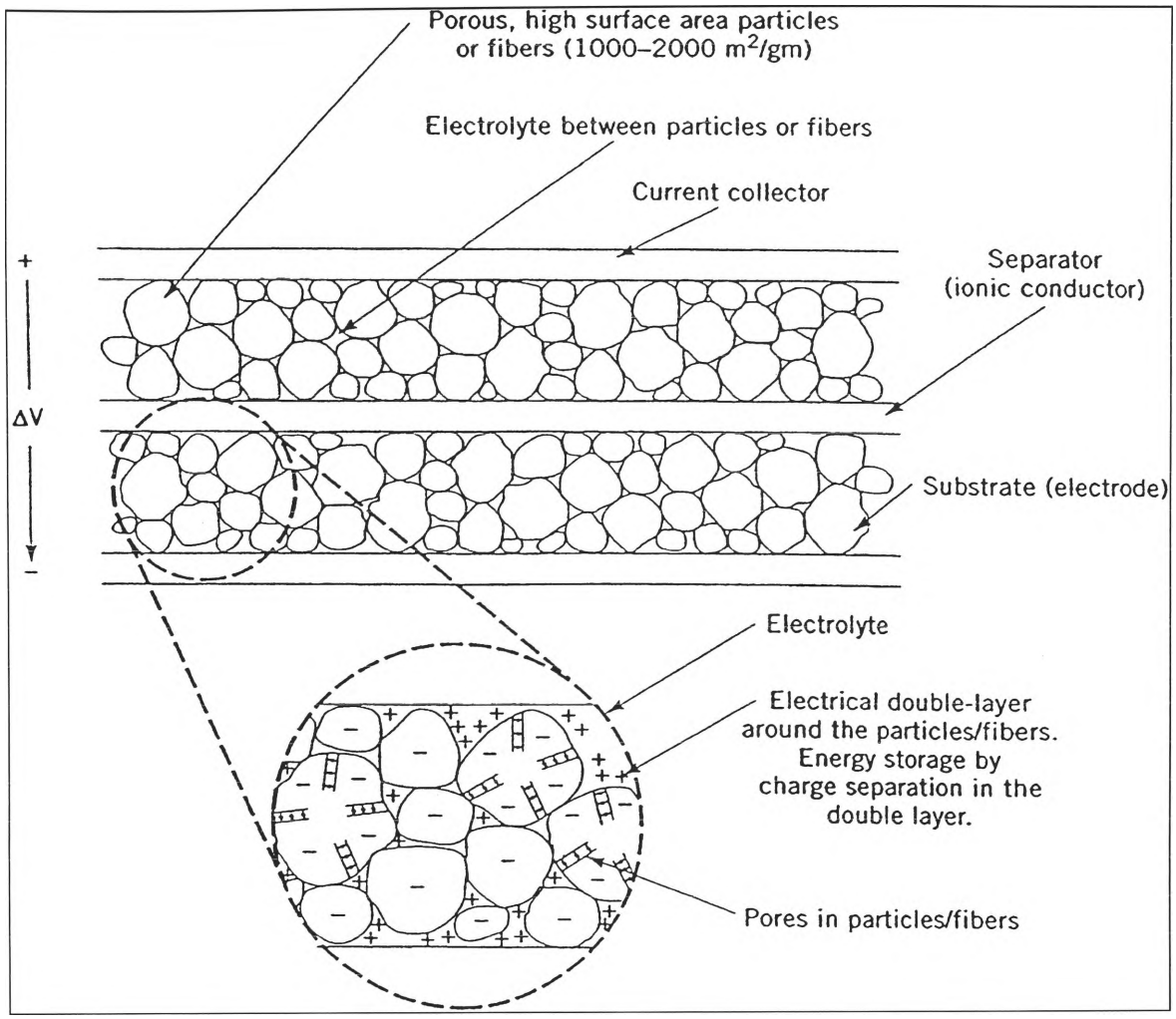

Figure 2-4. Schematic of a double-layer supercapacitor [3].

The thickness is very small for the double-layer (a fraction of 1 nm in liquid electrolytes), resulting in a high value for the specific capacitance of 15–30 μF cm^{-2}. If the surface area of the electrode is 1000 m^2 g^{-1}, the potential capacitance would go up to 150–300 F g^{-1} of electrode material. However, as indicated in Table 2-1 [3], the measured specific capacitances of the carbon materials current being used in supercapacitors are not as good as they are supposed to be. The values of the specific capacitance are in the range of 75–175 F g^{-1} for aqueous electrolytes and 40–100 F g^{-1} for organic electrolytes. This is

due to a relatively large fraction of surface area in the pores of the carbon materials that cannot be accessed freely by the ions in the electrolyte. This is especially true for the organic electrolytes, as the size of ions for the organic electrolytes is much larger than in the case of an aqueous electrolyte. In order to gain effective access within the pores, porous carbons for use in supercapacitors should have a large fraction of their pore volume in pores of diameter 1–5 nm in diameter. Materials with small pores (<1 nm) often encounter a large fall-off in capacitance when discharge currents are greater than 100 mA cm^{-2}, especially when organic electrolytes are used, while with the larger pore diameters, materials have a minimal decrease in capacitance when discharged at current densities of greater than 500 mA cm^{-2}.

Table 2-1. The specific capacitance of selected electrode materials [3].

Material	Density (g/cm^3)	Electrolyte	F/g	F/cm^3
Carbon cloth	0.35	KOH	200	70
		organic	100	35
Carbon black	1.0	KOH	95	95
Aerogel carbon	0.6	KOH	140	84
Particulate from SiC	0.7	KOH	175	126
		organic	100	72
Particulate from TiC	0.5	KOH	220	110
		organic	120	60
Anhydrous RuO_2	2.7	H_2SO_4	150	405
Hydrous RuO_2	2.0	H_2SO_4	650	1300
Doped conducting polymers	0.7	organic	450	315

The electrolyte is extremely important to supercapacitors, as the cell voltage of the supercapacitor is dependent on the electrolyte used. Normally, for aqueous electrolytes, the cell voltage is about 1 V, and for organic electrolytes, the cell voltage is up to 3–3.5 V.

2.2.2 Supercapacitors Utilizing Pseudocapacitance

For an ideal double-layer capacitor, the capacitance remains a constant and is independent of voltage, as the charge transfer goes into the double-layer and no faradaic reactions are involved between the electrode material and the electrolyte. However, for supercapacitors utilizing pseudocapacitance, most of the charge is transferred at the surface or in the bulk near the surface of the solid electrode material. The interaction between the solid material and the electrolyte involves faradaic reactions, described as charge transfer reactions. As the charge transferred during these faradaic reactions is voltage-dependent, the pseudocapacitance related to the faradaic reactions is also voltage-dependent. There are three types of electrochemical processes applied in the development of supercapacitors using pseudocapacitance. These are surface adsorption of ions from the electrolyte, redox reactions involving ions from the electrolyte, and the doping and undoping of the active conducting polymer material in the electrode [3]. The first two processes are primarily surface mechanisms, which are highly dependent on the surface area of the electrode material. The third one is a bulk process, involving the conducting polymer material. Although the electrode materials provide relatively high

surface area because of their micropores, which allow distributions of the ions to and from the electrodes in a cell, the specific capacitance of the material is much less dependent on its surface area. The electrodes must have high electronic conductivity in all cases in order to distribute and collect the electron current. The specific capacitance can be determined by cyclic voltammetry, which will be explained later.

As shown in Table 2-1, pseudocapacitance materials yield much higher values of specific capacitance than carbon materials. It is expected that the energy density from supercapacitors applying pseudocapacitance materials would also be higher.

2.2.3 Hybrid Capacitors

As a different type from normal supercapacitors, supercapacitors can also be fabricated with one electrode of a double-layer carbon material and the other electrode of a pseudocapacitance material (Fig. 2-5). Such devices are often called hybrid capacitors. Up to now, nickel oxide has been used as the pseudocapacitance material in the positive electrode for most of the hybrid capacitors. The energy density can be significantly higher for hybrid capacitors than for double-layer capacitors, but the limitation is that hybrid capacitors have nonlinear charge-discharge characteristics. Two non-similar mixed metal oxide or doped conducting polymer materials are also possible options to assemble hybrid capacitors.

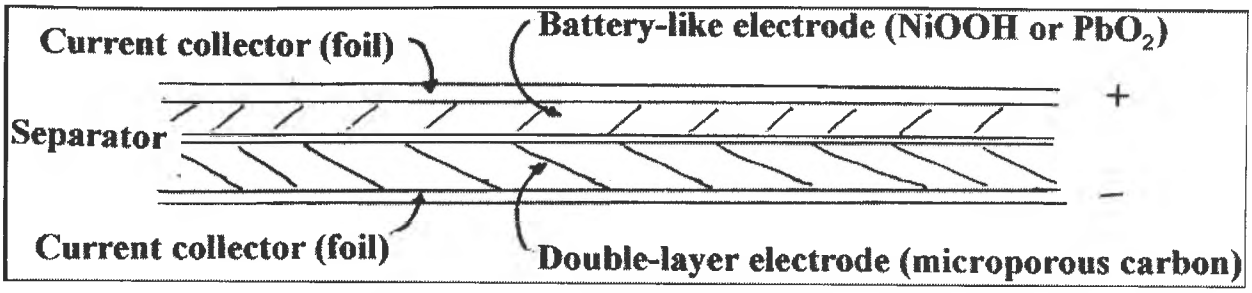

Figure 2-5. Schematic of a hybrid supercapacitor [3]

Current research in the United States, Japan, and Europe is making rapid progress, and the applications are mainly directed toward electric and hybrid vehicles, as well as for medical and consumer electronics. However, only a few of the devices are ready or near ready for commercialization, and even fewer are available for purchase even in small quantities.

In the following section, the present research status of supercapaciotr technology is reviewed for different types: carbon double-layer capacitors, supercapacitors utilizing pseudocapacitance, and hybrid capacitors. For each type, several examples are given for an overview.

2.3 Present Status of Supercapacitor Technology

2.3.1 Carbon Double-layer Capacitors

Activated carbon-based supercapacitors are the first such related materials applied in supercapacitors. The advantages of activated carbons are due to their low cost, large capacitance, and good cycling stability, which make them the most highly developed technology. In these devices the charge storage is electrostatic, and the electrolyte ions are reversibly adsorbed in the electrochemical double-layer of the porous carbon electrode structure [14].

As carbon nanotubes (CNTs) have special internal structures, high surface area, remarkable chemical stability, and electronic conductivity, they have been considered and demonstrated to be excellent new material for electrodes in electrochemical energy storage and conversion devices, including supercapacitor electrodes. C. Du et al. published a paper in 2006, reporting the fabrication of multi-walled carbon nanotube (MWNT) thin films by an electrophoretic deposition technique [15]. The most important finding in their research is that the supercapacitors built from such thin film electrodes presented a superior frequency response, with a frequency "knee" at about 7560 Hz, 70 times higher compared to any "knee" frequency (100 Hz), which has so far been reported. Other researchers have reported on the electrochemical and cycling characterization of an activated carbon supercapacitor cell [16]. This cell contained microporous activated

carbon as the active material and *N*-butyl-*N*-methylpyrrolidinium bis(trifluoromethanesulfonyl) imide ($PYR_{14}TFSI$) ionic liquid as the electrolyte. 60 F g^{-1} capacitance was exhibited at a 20-mV s^{-1} scan rate, with a maximum operating potential range of 4.5 V at 60 °C in CV measurements in their research. This capacitor maintained high cycling stability for 40,000 cycles without any change in the cell resistance (9 Ω cm^2) and a voltage up to 3.5 V at 60 °C, when assembled in a coin cell. Such high performance makes these sorts of capacitors suitable candidates for potential high temperature applications (≥60 °C).

2.3.2 Capacitors Utilizing Pseudocapacitance

2.3.2.1 Metal Oxide Capacitors

Like the activated carbons, transition metal oxides on the nanoscale often show high electrochemical activity and good discharge performance due to their high specific surface areas. Many transition metal oxides have been evaluated and investigated for their capabilities as supercapacitor electrodes. However, so far the high cost of the ruthenium oxide that exhibits the highest capacitance values remains an obstacle in making the supercapacitor technology commercially viable. This has led to studies of combinations of ruthenium oxide with other metal oxides, as well as mixed metal oxides. One example is the reported synthesis of a nanoscale SnO_2-V_2O_5 mixed oxide by a simple hydrothermal method [17]. When this SnO_2-V_2O_5 is combined with carbon nanotubes (CNT), the

SnO_2-V_2O_5-CNT electrode shows excellent performance from cyclic voltammetry measurements, about 121.4 F g^{-1}, at a scan rate of 100 mV s^{-1} in 0.1 M KCl solution. Another method is to develop low cost nanocrystalline and amorphous transition metal oxide electrodes for supercapacitors by employing innovative solution-based chemical synthesis procedures. Electrodeposition synthesis of nanostructured γ-MnO_2 films was achieved by Jun Chen's research group [6]. In their paper, they reported a combination of potentiostatic and cyclic voltammetric electrodeposition techniques to prepare carambola-like γ-MnO_2 nanoflakes on nickel sheets. This thin film is about 20 nm in thickness and at least 200 nm in width. The as-prepared MnO_2 nanoflake films displayed high specific capacitance in electrochemical measurements. There were indications that the carambola-like γ-MnO_2 nanoflakes could have potential applications in supercapacitors due to the capacitance of 240 F g^{-1} measured at the current density of 1 mA cm^{-2}.

2.3.2.2 Conducting Polymer Capacitors

Conducting polymers have attracted much interest in the supercapacitor field because of their high charge density (compared with carbon) and low cost (compared with metal oxides). In high surface area carbons, the charge separation of electronic and ionic charges at the interface between the electrode material and the electrolyte solution is the basic principle for energy storage. Hence, these sorts of capacitors are called 'electric double-layer' capacitors. In conducting polymers and in metal oxides, fast faradaic

charge transfer takes place at the electrode material, resulting in so-called 'redox' or 'pseudocapacitance' processes. After the charge-transfer process, the doping process, the polymers become electronically conductive [13, 14, 18]. These are the energy storage principles for conducting polymers.

Sivaraman et al. reported the preparation of an all-solid capacitor [19]. This kind of supercapacitor consists of polyaniline as the electrode material and sulfonated poly(ether ether ketone) (SPEEK) as the solid electrolyte. A composite electrode is made from chemically-synthesized polyaniline (Pani), sulfonated poly(ether ether ketone), electronically conducting carbon black, and polytetrafluoroethylene (PTFE). The unit cell consists of two p-dopable Pani composite electrodes, which are separated by a SPEEK membrane with a thickness of 50μm. Examined using cyclic voltammetry, charging–discharging, and impedance analysis, the unit cell capacitance was 0.6 F corresponding to 27 F g^{-1} of the active polymer material. Marina Mastragostino's group conducted some research into poly(3-methythiophene) [20]. They collected data on poly(3-methythiophene) positive and negative electrodes, and discussed the cyclability of supercapacitors with composite electrodes based on such conventional polymer. The capacitance and cycling stability of poly(3-methylthiophene) are sufficiently high to bring this polymer into consideration for supercapacitor technology.

2.3.2.3 Hybrid Capacitors

Development on hybrid capacitors has been conducted in Russia [21, 22], using nickel oxide as the positive, battery-like electrode, with some work done on using lead oxide [23] as the positive electrode material. In these hybrid capacitors, activated carbon cloth was used for the fabrication of the negative electrodes. The hybrid capacitors made in Russia have capacitances of 3000–15,000 F $cell^{-1}$, resulting from relatively thick electrodes. The Russian hybrid devices perform more like a battery rather than a supercapacitor. In most applications, the charge and discharge times would be 10–20 min and the peak power density for a high efficiency discharge would be about 300 W kg^{-1}. The energy density claimed for charge/discharge is about 1.5 W h kg^{-1} for 0.8–1.3 V and 8–10 W h kg^{-1} for 0.8–1.6 V in the case of the devices using nickel oxide, dependent on the voltage range. The large difference in energy density is due to the pseudocapacitance in the carbon electrode at the higher voltage. For the devices using lead oxide for the positive electrode, the energy density claimed is 10–20 W h kg^{-1} for a voltage range of 0.7–1.8 V. The Russian devices appear to be essentially high power batteries having a relatively low energy density rather than more traditional supercapacitors.

2.3.3 Solid-State Supercapacitors

Most of the redox supercapacitors reported [24-26] are based on liquid electrolytes. These supercapacitors with liquid electrolytes have the major disadvantages of corrosion,

self discharge, bulky design, and low energy density, similar to the case of liquid electrolyte batteries. To avoid these shortcomings, major attention has been recently devoted to the fabrication of so-called solid-state capacitors, which apply solid polymer or gel as electrolytes. This kind of electrolyte is selected to provide high ionic conductivity and advantageous mechanical properties, including flexibility for proper electrode–electrolyte interactions and the ability to form thin films of desirable area. The solid-state redox supercapacitors are the new generation of supercapacitors and have not been widely reported. A few studies have recently investigated different polymer or gel electrolytes, such as poly(methylmethacrylate) (PMMA)–ethylene carbonate (EC)–propylene carbonate (PC)–$LiClO_4$ (PMMA-EC-PC-$LiClO_4$) [27, 28], polyethylene glycol (PEG)–PC–tetraethyl ammonium tetrafluoroborate ($TEABF_4$) [29], polyethylene oxide (PEO)–PEG–$LiCF_3SO_3$ [30, 31], PVA–H_3PO_4 [30, 31], PMMA–EC–PC–$NaClO_4$ [32], etc.

2.4 Key Design and Cost Issues

In the past ten years of research and development of supercapacitors, significant progress has been made, but so far no device is available to meet all the requirements in both the technical and the economic aspects. In vehicle applications for example, it is required for a device to have high energy density (>5 Wh kg^{-1}), high power density (low resistance), long cycle and shelf life, and reasonably low cost (<US $2–3/Wh). There are several design issues to be considered, e.g. electrode thickness and material properties, contact resistance between material particles/fibers, bonding of the active materials to a current collector, electrolyte resistivity, cell/stack configuration, packaging, electrode material and electrolyte purity, quality and uniformity of fabrication, cost of materials, and so forth [3].

2.5 Summary

Batteries, fuel cells and capacitors are the three main types of energy storage devices that are widely used around the world. Supercapacitors have many advantages and fill the gap between batteries and regular capacitors. The most important characteristic of supercapacitors, unlike other types of capacitors, is their "super" high energy density. Several materials, such as activated carbon, transition metal oxides, and conducting polymers, are suitable candidates for supercapacitor electrode materials. Solid-state supercapacitors have been recently developed with solid-state electrolytes, which show advantageous features compared to normal liquid electrolytes. Although different energy storage mechanisms are applied for each type of device, the supercapacitors have promising applications, especially in vehicles.

Supercapacitor development is continuing worldwide, with good progress being made in improving their electrochemical performance. However, markets for supercapacitors have not been developed due primarily to their high cost and relatively low energy density. There are two key factors that could reduce the price. One is to utilize lower cost electrode materials, such as carbon blacks and low cost metal oxides, which will result in lower material costs. The other is to develop assembly processes that can be automated at reasonable investments.

Chapter 3. Experimental

3.1 Materials and Chemicals

A list of the names of materials or chemicals used in the research project is shown below in Table 3-1.

Table 3-1. Materials or chemicals used in the research project.

Materials or Chemicals	Formula	Purity	Supplier
Vanadium (V) Oxide	V_2O_5	98%	Sigma-Aldrich
Nitric Acid	HNO_3	69%	Sigma-Aldrich
Citric Acid	$HOC(COOH)(CH_2COOH)_2$	99.5%	Sigma-Aldrich
Carbon Black	C		Lexel
Polyvinylidene Difluoride (PVdF)		99%	Sigma-Aldrich
N-Methyl Pyrrolidinone (NMP)	C_5H_9NO		Sigma-Aldrich
Potassium Chloride	KCl	99%	Sigma-Aldrich
Cobalt Chloride Hexahydrate	$CoCl_2 \cdot 6H_2O$	98%	Sigma-Aldrich
Urea	$CO(NH_2)_2$	99.5%	Sigma-Aldrich
Cobalt (II, III) Oxide, <10 μm	Co_3O_4	99%	Sigma-Aldrich
Potassium Hydroxide	KOH	90%	Sigma-Aldrich
Iron (III) Trichloride	$FeCl_3$	97%	Sigma-Aldrich
Iron (III) Oxide	Fe_2O_3	97%	Sigma-Aldrich

Sodium Thiosulfate	$Na_2S_2O_3$	99%	Sigma-Aldrich

3.2 Materials Synthesis Techniques

3.2.1 Spray Pyrolysis

Spray pyrolysis is a powerful synthesis technique that can be used to produce a wide variety of chemically homogenous ceramic powders with high purity. Oxide powders with homogenous particle sizes and crystallite sizes less than 100 nm may be prepared by this method. Spray pyrolysis synthesis is simple and time-efficient, allowing for continuous operation. With the addition of a carbon source, oxide/carbon composites can be generated, giving extra benefits for electrochemical performance. The morphology of the particles produced by spray pyrolysis can (to some degree) be controlled by the choice of precursors, the concentration of the precursor solution, the size of the spray droplets, and the retention time in the furnace.

Fig. 3-1 presents a schematic of the spray pyrolysis system for the preparation of nanosized powders [33]. The working procedures are as follows. An initially prepared water-based precursor solution is fed through a nozzle into a rotating furnace, which has been preheated to the predetermined temperature. In the hot-zone, the atomized solution is dried and the metal salts decompose at a high temperature, forming an intimate metal oxide mixture. The spray pyrolysed powders are collected in a cyclone at the bottom of

the furnace and are then subjected to further treatment or characterizations.

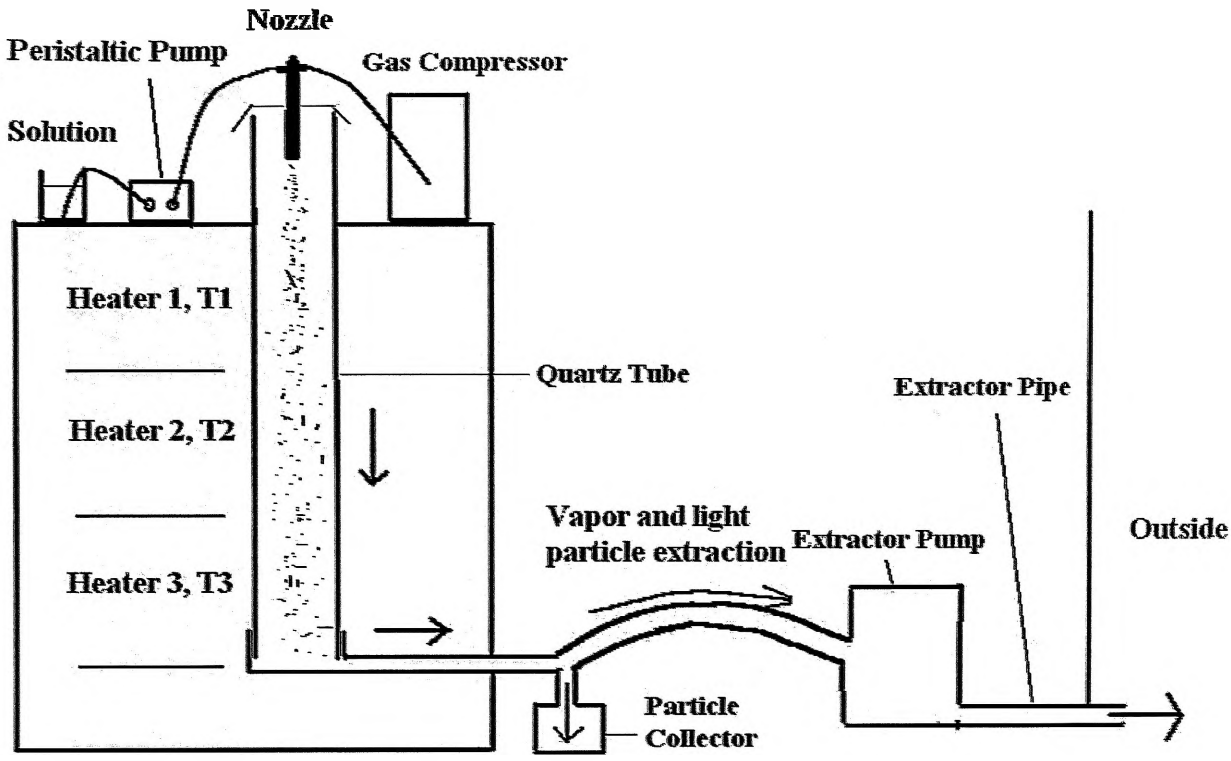

Figure 3-1. Experimental setup for preparing metal oxides by the pray pyrolysis technique [33].

3.2.2 Hydrothermal Synthesis

Hydrothermal synthesis is a method used to synthesize single crystals. The crystal is grown in hot water under high pressure, depending on the solubility of the precursors. The synthesis is performed in an apparatus called an autoclave, in which the 'nutrient' solution containing precursors for crystal growth is supplied along with water. A gradient of temperature is maintained at opposite ends of the growth chamber, so that the hotter end dissolves the nutrient and the cooler end facilitates growth of the crystal seeds.

A typical Teflon-lined autoclave is shown in Fig. 3-2 (left). Precursor solution would be initially prepared and filled into the autoclave. Then this autoclave is to be sealed in a stainless steel container (Fig. 3-2, right) and maintained at the aim temperature in an oven.

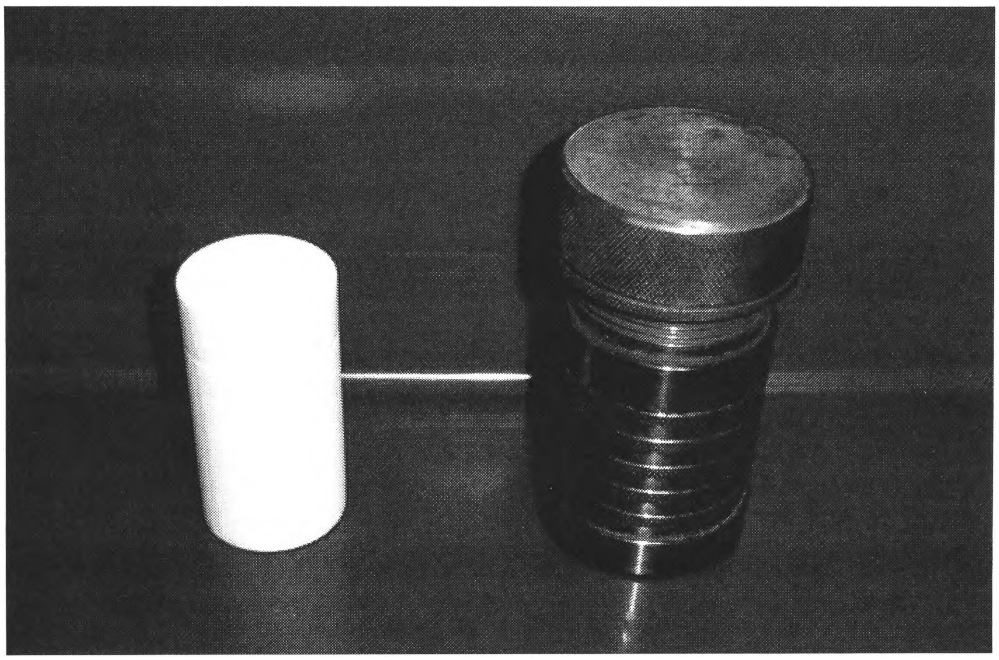

Figure 3-2. Experimental setup for hydrothermal synthesis: a Teflon-lined autoclave (left); and a stainless steel container (right).

There are several advantages of the hydrothermal method over other types of crystal growth. One is that crystalline phases which are not stable at the melting point can be created. Moreover, the growth of materials with a high vapour pressure near their melting points can be performed. Also, it is particularly suitable in that large good-quality crystals can be grown by the hydrothermal method while maintenance of composition control is needed. Possible disadvantages include the need for expensive autoclaves and good quality seeds of a fair size, and the impossibility of observing the crystal as it grows.

3.3 Materials Characterizations

3.3.1 X-ray Diffraction (XRD)

When a wave encounters a series of regularly spaced obstacles, diffraction will occur. These obstacles must satisfy the conditions that they are capable of scattering the wave and have spacings that are comparable in magnitude to the wavelength. Furthermore, as two or more waves are scattered by these kinds of obstacles, the specific phase relationships established between them will lead to the diffraction phenomena.

X-rays are a form of electromagnetic radiation with high energies and short wavelengths. The X-ray beam will be scattered in all directions when it impinges on a solid material. This is because of the electrons associated with each atom or ion that lies within the beam's path.

There are many diffraction techniques applied, among which the most common one is to employ a powdered or polycrystalline specimen consisting of many fine and randomly oriented particles. These particles are exposed to monochromatic X-ray radiation. Each powder particle (or grain) is a crystal, and there are a large number of them with random orientations. These orientations ensure that some particles are properly oriented so that every possible set of crystallographic planes will be available for diffraction.

To determine the crystal structure is one of the primary uses of X-ray diffractometry. As a particular arrangement of atoms within the unit cell leads to particular relative intensities of the diffraction peaks, the unit cell size and geometry may be resolved from the angular positions. X-rays are also used in other types of material investigations and applications. For example, crystallographic orientations of single crystals can be deduced using X-ray diffraction (or Laue) photographs. Other uses of X-rays are in the field of qualitative and quantitative chemical identifications, as well as the determination of residual stresses and crystal size [34].

3.3.2 Scanning Electron Microscopy (SEM) & Transmission Electron Microscopy (TEM)

Electron diffraction is a technique used to study matter. When electrons are fired at a sample, the resulting interference pattern can be observed. This is due to the wave-particle duality, meaning that an electron can be regarded as a wave. This technique is similar to X-ray diffraction and neutron diffraction. Electron diffraction is usually performed in a transmission electron microscope (TEM) or a scanning electron microscope (SEM) as electron backscatter diffraction, to study the crystal structure of solids. At first, the electrons are accelerated by an electrostatic potential. This will result in the desired energy and wavelength for the electrons before they interact with the sample to be studied. The periodic structure of a crystalline solid acts as a diffraction grating, scattering the electrons in a predictable manner. It may be possible to deduce the structure of the crystal from the observed diffraction pattern. However, the technique is

limited by the phase problem.

Compared with other types of radiation used in diffraction studies of materials, such as X-rays, the main difference lies in the fact that electrons are charged particles and interact with matter via the Coulomb forces. This means that the incident electrons feel the influence of both the positively charged atomic nuclei and the surrounding electrons. In comparison, X-rays interact with the spatial distribution of the valence electrons. Because of these different forms of interaction, the two types of radiation are suitable for different studies. Electron diffraction will give high resolution at the nanometer scale, while X-ray diffraction is of relatively low resolution.

As mentioned above, the wavelength of electrons accelerated in a TEM is much smaller than that of the radiation usually used for X-ray diffraction experiments. A consequence of this is that the radius of the Ewald sphere is much larger in electron diffraction experiments than in X-ray diffraction. This allows the diffraction experiment to reveal more of the two dimensional distribution of reciprocal lattice points.

3.3.3 Brunauer-Emmett-Teller (BET) Technique and Pore Size Distribution

The Langmuir isotherm will not be valid when molecules form multilayers. To take this possibility into account, in 1938, Stephan Brunauer, Paul Emmett, and Edward Teller developed a model isotherm. The theory is called BET Theory, from the initials of their

last names. The BET theory is used to calculate the specific surface area (m^2 g^{-1}) of the materials from N_2 adsorption isotherms.

The pore size distribution, on the other hand, applies the gas adsorption isotherms to describe the distribution of pore volume with respect to pore size; alternatively, it may be defined by the related distribution of pore area with respect to pore size.

3.3.4 Thermogravimetric Analysis (TGA)

Thermogravimetric Analysis (TGA) is a type of testing to determine changes in weight of samples in relation to changes in temperature. This analysis is dependent on a high degree of precision in three measurements: weight, temperature, and temperature change. TGA is commonly employed in research and testing to determine characteristics of materials such as polymers, to determine degradation temperatures, absorbed moisture content of materials, the level of inorganic and organic components in materials, the decomposition points of explosives, and solvent residues. It is also often used to estimate the corrosion kinetics in high temperature oxidation.

3.4 Electrochemical Testing

3.4.1 Electrode Preparation

Most electrodes of batteries or supercapacitors are a complex composite of powders composed of particles of the active material, a conductive diluent (usually carbon or metal powder), and a polymer binder to hold the mix together and bond the mix to a conductive current collector. Typically, a composite battery electrode has 30% porosity with a complex surface extending throughout the volume of the porous electrode. This yields a much greater surface area for reaction than the geometric area and reduces polarization. The pores of the electrode structures are filled with electrolyte. In the case of electrodes of batteries and supercapacitors in the ISEM laboratories, 60-70 wt% active material, 20-30 wt% carbon black, and ~10 wt% PVdF binder are to mixed together with NMP to make a slurry pasted on a substrate (platinum foils for supercapacitor electrodes). Then, the electrode is heated in a vacuum oven at 110 °C or 120 °C overnight to remove the organic binder.

3.4.2 Cyclic Voltammetry

Cyclic voltammetry (CV) is a type of potentiodynamic electrochemical measurement, in which the working electrode potential is ramped linearly versus time like linear sweep voltammetry. The working electrode's potential ramp is inverted, when the cyclic

voltammetry reaches a set potential. This inversion can happen multiple times during a single experiment. The current at the working electrode is plotted against the applied voltage to give a cyclic voltammogram showing the trace of current vs. voltage. Cyclic voltammetry is generally used to examine the electrochemical properties of an analyte in solution.

An analyte with redox activity within the experimental potential window is important to the utility of cyclic voltammetry measurements. It is also highly desirable for the analyte to exhibit a reversible wave, which is when an analyte is reduced or oxidized on a forward scan and it can be then re-oxidized or re-reduced in a predictable way on the return scan.

The method uses a three-electrode set-up with a reference electrode, a working electrode, and a counter electrode working in combination. For supercapacitors, the three-electrode test cell consists of one working electrode (with the active electrode material), one counter electrode (a large piece of platinum foil), and one reference electrode (Saturated Calomel Electrode, SCE). Inorganic compounds or organic conducting polymers often act as the electrolytes, in which these three electrodes are immersed. The electrolyte is usually added to the test cell to ensure sufficient conductivity. The combination of the solvent, electrolyte, and specific working electrode active material determines the range of the potential window for the CV measurements.

The specific capacitance of the active material can be computed from the CV curve using the relationship shown below. The area under the current–potential curve can be estimated by integration, and then the area is divided by the sweep rate (V s^{-1}), the mass of active material of the electrode (g), and the potential window (V), giving a specific capacitance in F g^{-1}:

$$C = \frac{I}{mv(Va-Vc)} \int_{Va}^{Vc} I(V)\, dV \qquad (3\text{-}1)$$

where $(V_a - V_c)$ represents the potential window.

Chapter 4. Vanadium Pentoxide/Carbon Nanocomposites as Electrode Materials for Electrochemical Capacitors

4.1 Introduction

Vanadium oxides have significant uses in energy-related devices [35-37] due to their phase transformations. V_2O_5 has attracted great interest because it has potential applications in optical switch devices [38], electrochromic devices [39-41], and as a reversible cathode material for lithium batteries [42, 43]. Due to its low cost and ability to exist in different oxidation states, this compound is also a promising electrode material for electrochemical capacitor applications. In fact, there have already been quite a few investigations into V_2O_5 as an electrode active material for electrochemical capacitors. Initially, V_2O_5 was prepared by quenching V_2O_5 fine powders at 950 °C in a bath of de-ionized water [44]. The specific capacitance was 346 F g^{-1} in an electrolyte with a pH of 2.32. Later, nanoporous layer-structured V_2O_5 was prepared by the sol-gel method [45]. The maximum specific capacitance was reported to be 214 F g^{-1}. In a previous study [46], nanocrystalline V_2O_5 powders were prepared by co-precipitation and calcination. The specific capacitance of the V_2O_5 powders was 262 F g^{-1}, which was obtained in 2 M KCl electrolyte at a 5-mV s^{-1} scan rate.

In the work shown here, improved electrochemical performance of V_2O_5 has been achieved by synthesis of a V_2O_5/carbon composite using the spray pyrolysis method. Spray pyrolysis is a powerful tool for synthesizing large quantities of high-purity oxide

powders with homogeneous nanosized crystals [47-49]. The resultant V_2O_5/carbon composite powders were systematically tested and electrochemically evaluated for their specific capacitance. The role of carbon in the composite is also considered and discussed.

4.2 Experimental

18.188 g of commercial V_2O_5 powders were dissolved in 500 ml of nitric acid (diluted four times from 69% nitric acid), followed by the addition of 20 g of solid citric acid (giving 29.7 wt% carbon in the total mass of V_2O_5 and carbon) under heating and rigorous stirring to prepare the solution. A homogeneous solution was obtained and was marked by a color change from yellow to green to blue. Then, the resultant 0.2 M blue solution was sprayed at a temperature in the range of 450-500 °C in the spray pyrolysis system. Yellowish brown powders were generated from this procedure and then collected. The temperature range was limited by the facts that at 400 °C the material is still amorphous and that at 550 °C all of the carbon has left the system and no composite material can be found.

The as-prepared powders were characterized by XRD using a GBC MMA X-ray diffractometer with Cu K_α and graphite monochromator. The powder morphology, structure, and microchemistry were investigated by SEM (JEOL 6460 Scanning Electron Microscope), TEM and high-resolution TEM (HRTEM, JEOL 2011 200 keV analytical

instrument with a JEOL energy dispersive spectroscopy (EDS) detector). TEM samples were prepared by dispersion of as-prepared powders onto holey carbon support films. TGA was conducted with a TA Q500 Thermogravimetric Analyzer to detect the weight loss of the powders at 5 °C min^{-1} in air for temperatures up to 600 °C, from which the carbon content was determined. The specific surface area of the powders was determined by the gas sorption technique using a Quanta Chrome Nova 1000 Gas Sorption Analyzer based on the BET method. N_2 adsorption isotherms were obtained on the same facility to analyze the pore size distributions for the as-prepared powders.

Electrochemical testing was performed on an Electrochemical Workstation (CHI 660C), using the CV technique to investigate the specific capacitance of the resultant V_2O_5/carbon powders. Beaker-type three-electrode test cells were fabricated. The working electrode was made by dispersing 64.9 wt% V_2O_5/carbon material, 26.5 wt% carbon black, and 9.6 wt% PVdF binder in NMP solvent to form a slurry, which was then spread onto platinum foil. A platinum foil and a saturated calomel reference electrode (SCE) were used as the counter electrode and the reference electrode, respectively. The electrolyte was a 2-M KCl aqueous solution. CV was conducted over a voltage range from –0.2 V to 0.7 V at various scan rates (5 mV s^{-1}, 10 mV s^{-1}, 20 mV s^{-1}, and 50 mV s^{-1}).

4.3 Results and Discussion

It is well known that vanadium has various oxidation states: +2, +3, +4, and +5 with different colors displayed (V^{5+}: yellow; V^{4+}: blue; V^{3+}: green; V^{2+}: violet). A yellowish color was observed initially in the solution preparation as V_2O_5 was acidified by dilute nitric acid and VO_2^+ (yellow +5 oxidation number) was produced. Then VO_2^+ was reduced to blue VO^{2+} in the presence of citric acid, which acted as a weak reduction agent. It can be seen that during the reaction, the solution first became green, as a mixture of the original yellow of the +5 state and the blue of the +4 was present. As the reaction continued, the mixture turned blue, suggesting that all +5 state vanadium ions had converted to the +4 state, which resulted in a blue homogeneous solution.

4.3.1 Characterizations

Typical XRD patterns for the as-prepared powders are shown in Fig. 4-1. The powders sprayed at 450 °C consisted of nanocrystalline V_2O_5 phase, which can be indexed as Shcherbinaite, with an orthorhombic structure (PDF card 41-1426), as shown in Fig. 4-1(a). The average size of the V_2O_5 crystallites was estimated by the well-known Scherrer formula to be about 40 nm. The carbon in the system remains amorphous and is not present in significant enough quantities to be detected by XRD. Fig. 4-1(b) presents the XRD pattern of the product obtained at 500 °C. The XRD pattern is similar, and the estimated average crystal size based on peak broadening is now about 50 nm. The higher

value is believed to be associated with increased particle coarsening at the higher spraying temperature.

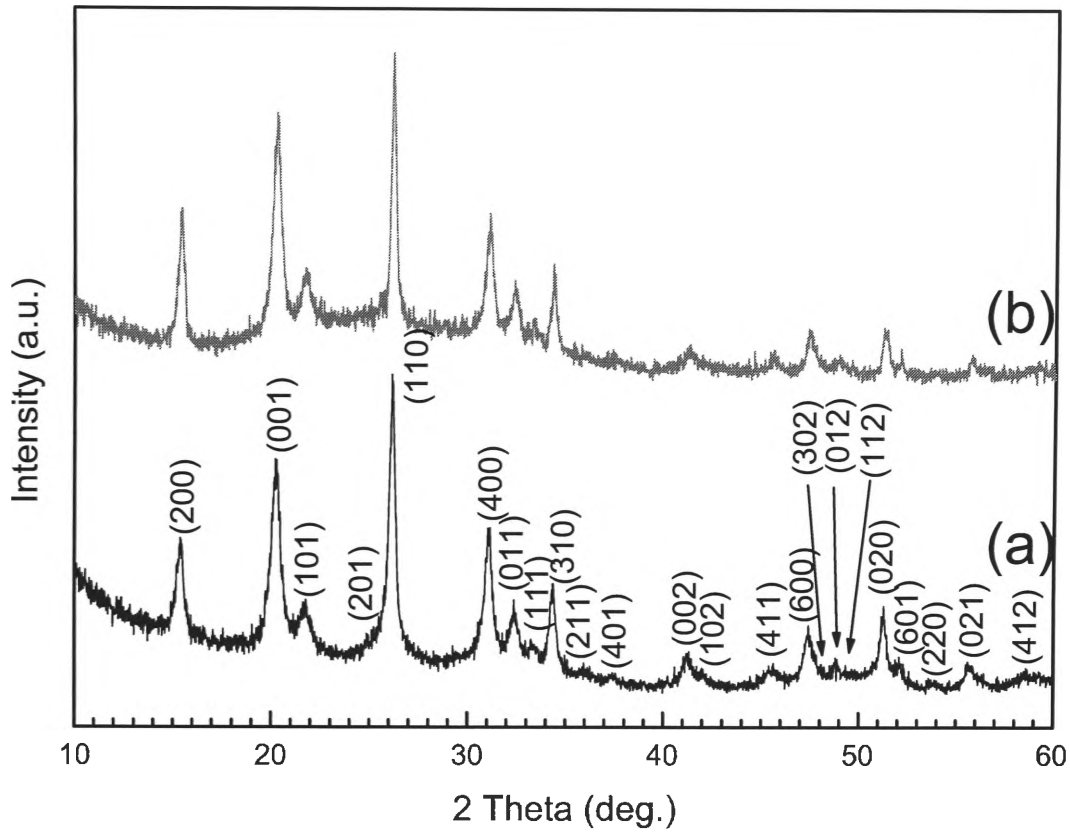

Figure 4-1. X-ray diffraction patterns of as-prepared V_2O_5/carbon powders: (a) sample sprayed at 450 °C; (b) sample sprayed at 500 °C.

Morphological features of the V_2O_5/carbon powders detected by SEM are shown in Fig. 4-2. The powders sprayed at 450 °C consisted mostly of hollow spheres (Fig. 4-2(a)), with average sphere diameters less than 10 μm. The image shown in Fig. 4-2(b) indicates a specific morphology of whiskers, later confirmed by TEM to comprise rod and ribbon-shaped nanoparticles, dispersed through the whole shell surface and extending

outwards. The existence of these long nanoparticles and the open structure would have benefits for ionic diffusion throughout the electrode surface in electrochemical measurements. The SEM images of powders sprayed at 500 °C are shown in Fig. 4-2(c) and 4-2(d). In contrast to the product obtained at 450 °C, there was no evidence of long nano-whiskers. The small pores in the spheres that are visible in the SEM images are due to the release of CO_2 gas in the spray pyrolysis process.

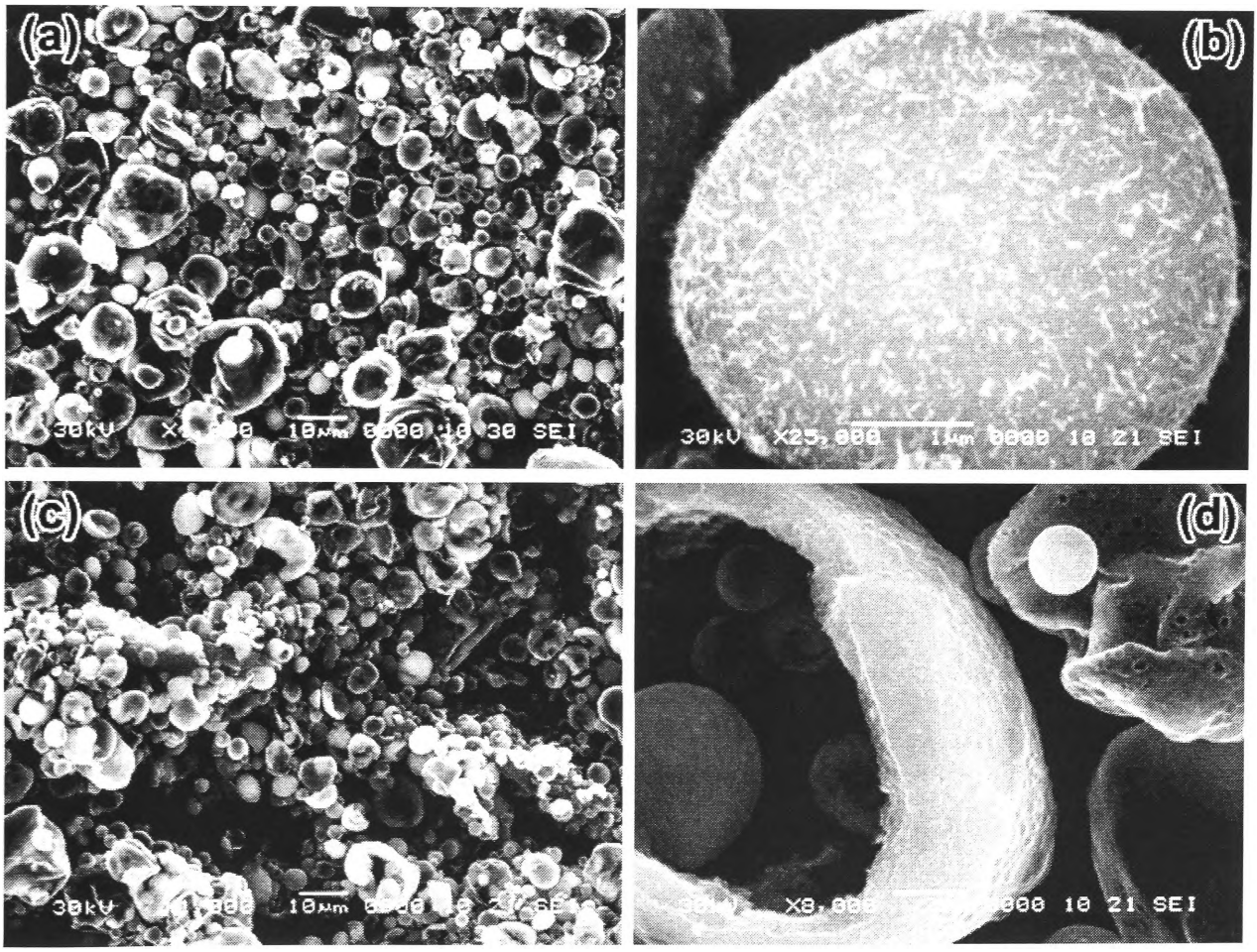

Figure 4-2. SEM images of as-prepared V_2O_5/carbon composite powders: (a) and (b) product obtained at 450 °C; (c) and (d) product obtained at 500 °C.

Detailed TEM and HRTEM observations of the sample sprayed at 450 °C are shown in Fig. 4-3. Low magnification bright field imaging (Fig. 4-3(a) and 4-3(b)) confirmed the presence of hollow, spherical shell agglomerates, with average diameters of ~0.3-3 μm. Examination by EDS of the agglomerated regions, which were located over holes in the carbon support film, confirmed the presence of V, O, and C (Fig. 3(a)), with semi-quantitative analysis consistent with a V:O atomic ratio of 2:5 and an average of 2-3 wt% carbon, depending on the local region (>50 nm diameter) examined. Intermediate magnification examination of features within the shells revealed a network of interwoven nanoribbons (Fig. 4-3(c)) and nanorods (Fig. 4-3(d)). This network was not fully dense, as indicated in Fig. 4-3(d)), allowing for ease of ionic diffusion. Examination of the outer regions of the shells confirmed that the fine whiskers observed in SEM images were in fact a mixture of thin nanorods and nanoribbons. Dark-field imaging (Fig. 4-3(f)) combined with selected area electron diffraction (inset, Fig. 4-3(f)) confirmed that the nanostructure comprised thin rod and ribbon-shaped V_2O_5 crystallites, with most sizes indicated by dark-field imaging to be within the range of 5-150 nm. This was also confirmed for longer ribbons and rods extending from the outside of the spheres. High-resolution TEM imaging also produced contrast consistent with the presence of fine V_2O_5 nanorods, which were located in a fairly uniform dispersion of amorphous carbon (Fig. 4-3(g)). For example, the crystal fringes marked in Fig. 4-3(g) have a spacing consistent with (1 0 1) V_2O_5. Contrast associated with the amorphous carbon alone is indicated in the marked region of Fig. 4-3(h), while contrast consistent with the formation of V_2O_5 ((0 1 0) fringes) and amorphous carbon in regions protruding from the

spheres is shown in Fig. 4-3(i) and its associated Fourier transform image (consistent with (0 1 0) fringes, d_{hkl} = 0.438 nm).

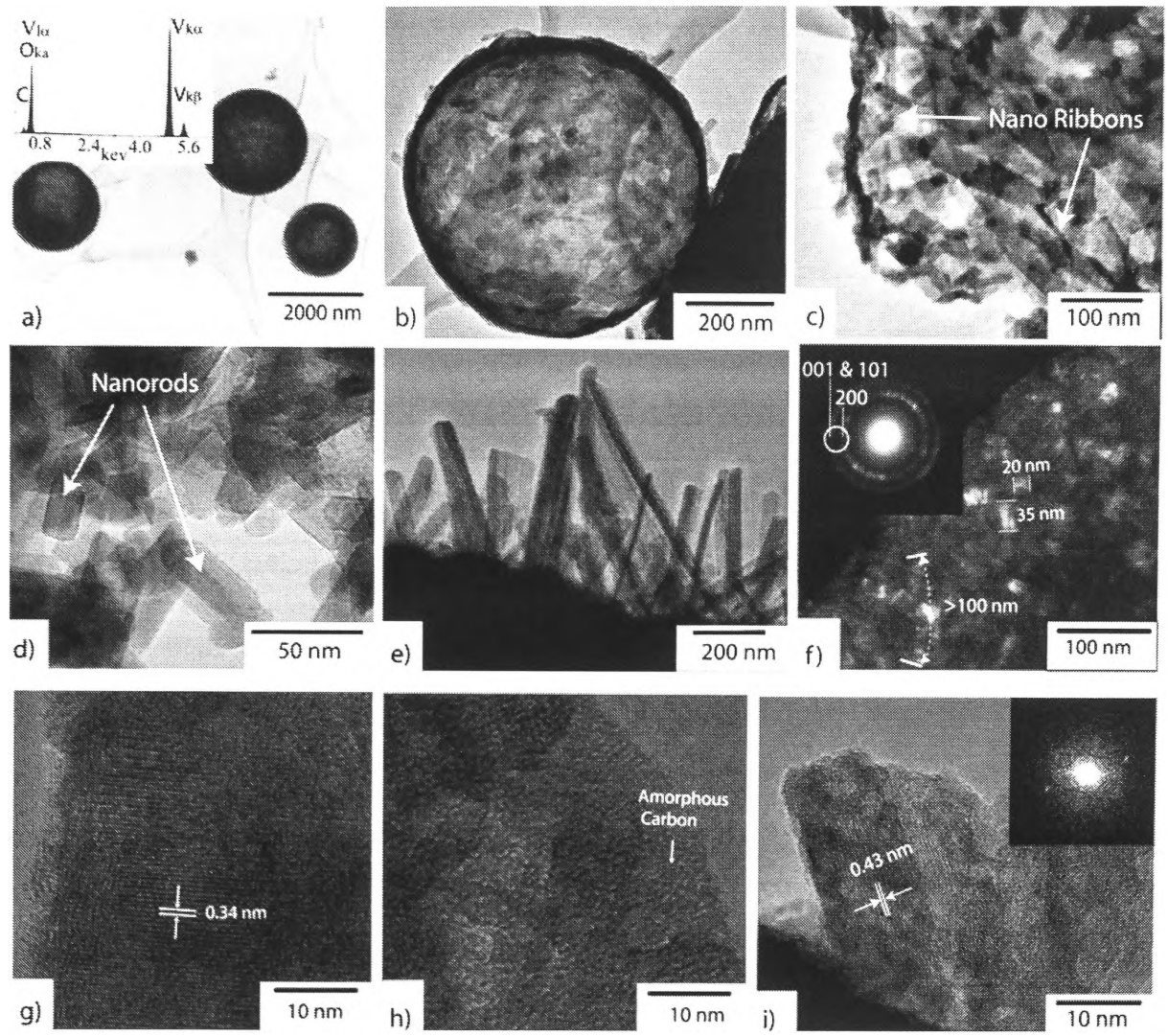

Figure 4-3. TEM and HRTEM images obtained from the V_2O_5/carbon composite powders sprayed at 450 °C:
(a) low magnification image and typical EDS spectrum (inset) obtained from a particle region not supported by holey carbon;
(b-e) morphological features revealed by bright field imaging;
(f) dark-field image of V_2O_5 nanorods obtained using circled V_2O_5 reflections, as indicated in the selected area electron diffraction pattern (inset);
(g-i) high resolution images with V_2O_5 nanorods and nanoribbons dispersed in amorphous carbon;
(i) V_2O_5 nanorods protruding from surface and associated Fourier transform diffractogram. (Fringes in (g) are due to V_2O_5 (1 1 0), fringes in (i) are V_2O_5 (0 1 0).)

TGA analysis of the V_2O_5/carbon materials is shown in Fig. 4-4. The samples obtained at 450 °C and 500 °C were preheated in vacuum at 120 °C for 24 h to ensure the removal of any water prior to the measurement. The maximum temperature was set at 600 °C to avoid decomposition of the V_2O_5 powders. The minimal weight loss from room temperature to 120 °C for both samples is due to the remaining traces of absorbed water. The observed additional weight losses for both samples in the temperature region of 120 -490 °C could be ascribed to the decomposition of species containing carbon in amorphous form (according to the HRTEM) or partially decomposed and polymerized citric acid. For powders sprayed at 450 °C (Fig. 4-4(a)), the weight loss is about 2.7 wt% which is close to the EDS result (2-3 wt%) estimating the total carbon content in the composite. From 490 °C to 600 °C, the weight remained the same, as no thermal reaction occurred. The TGA curve of the V_2O_5/carbon composite sprayed at 500 °C is similar, but the weight loss in the temperature range 120-490 °C is less – about 1.6 wt %, which is due to the promotion of carbon oxidation and CO_2 release at 500 °C during the spray process (Fig. 4-4(b)).

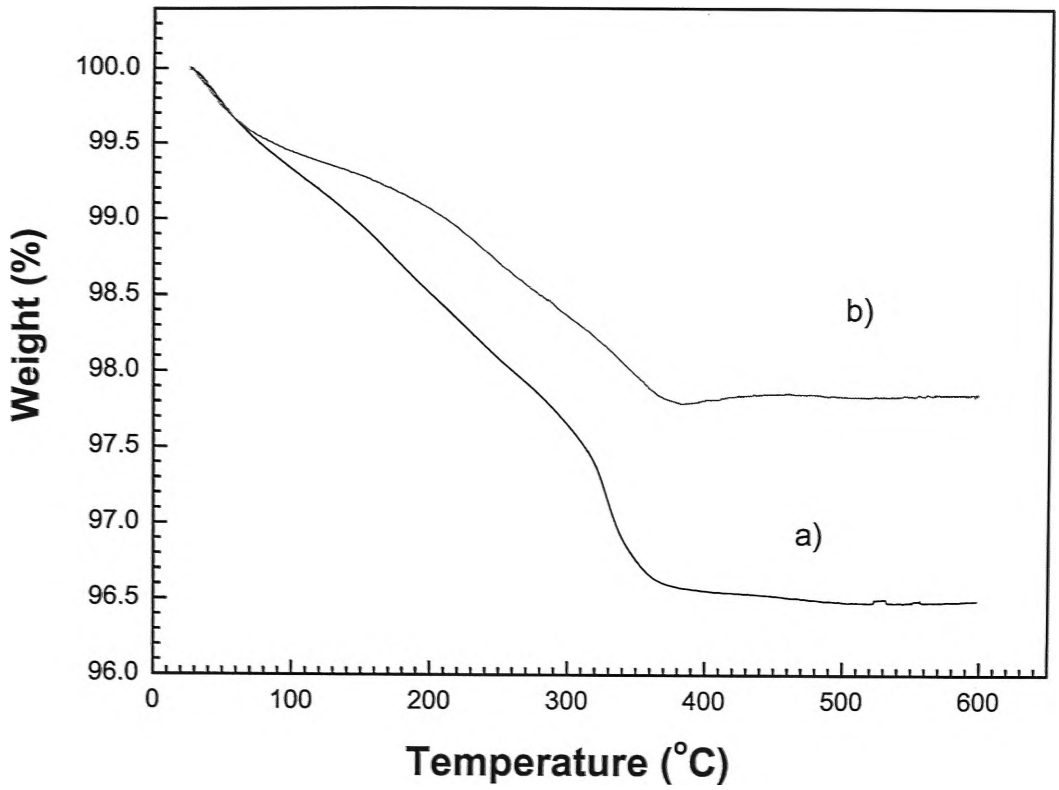

Figure 4-4. TGA curves of as-prepared V_2O_5/carbon powders in the temperature range from room temperature to 600 °C: (a) sample sprayed at 450 °C; (b) sample sprayed at 500 °C.

Multiple-point BET measurements showed that the as-prepared V_2O_5/carbon composite powders have specific surface areas of 18 m^2 g^{-1} and 26 m^2 g^{-1} when sprayed at 450 °C and 500 °C, respectively. The specimen obtained at the lower spray temperature (450 °C) had a smaller specific surface area, compared to that at 500 °C. This is due to the additional carbon oxidation and release of CO_2 gas at the higher temperature, leading to increased porosity. More holes and defects would be present when the precursor solution was sprayed at the higher temperature. Combined with additional TEM investigations, it

is clear that the V_2O_5/carbon powders obtained at 450 °C exhibit a unique open nano-network, consisting of nanorods and nanoribbons, which would not be so helpful for high values of the specific surface area, as they are present in tiny amounts. Nevertheless, the network provides gaps and voids, and might have benefits for electrochemical performance. Pore size distribution curves (Fig. 4-5) were plotted, based on the N_2 adsorption isotherms. Compared to composite powders generated at 500 °C, the product at the lower spray temperature (450 °C) has larger pores, with diameters of 40-50 Å, as shown in Fig. 4-5(a). These pores would allow easier ionic diffusion and interactions between the electrode and electrolyte. Smaller pores were present, with diameters in the range of 20-40 Å (Fig. 4-5(b)). These were accompanied by holes and defects in the as-prepared V_2O_5/carbon composite at 500 °C, which is the reason for the relatively larger specific surface area of 26 $m^2 g^{-1}$ from the BET measurements.

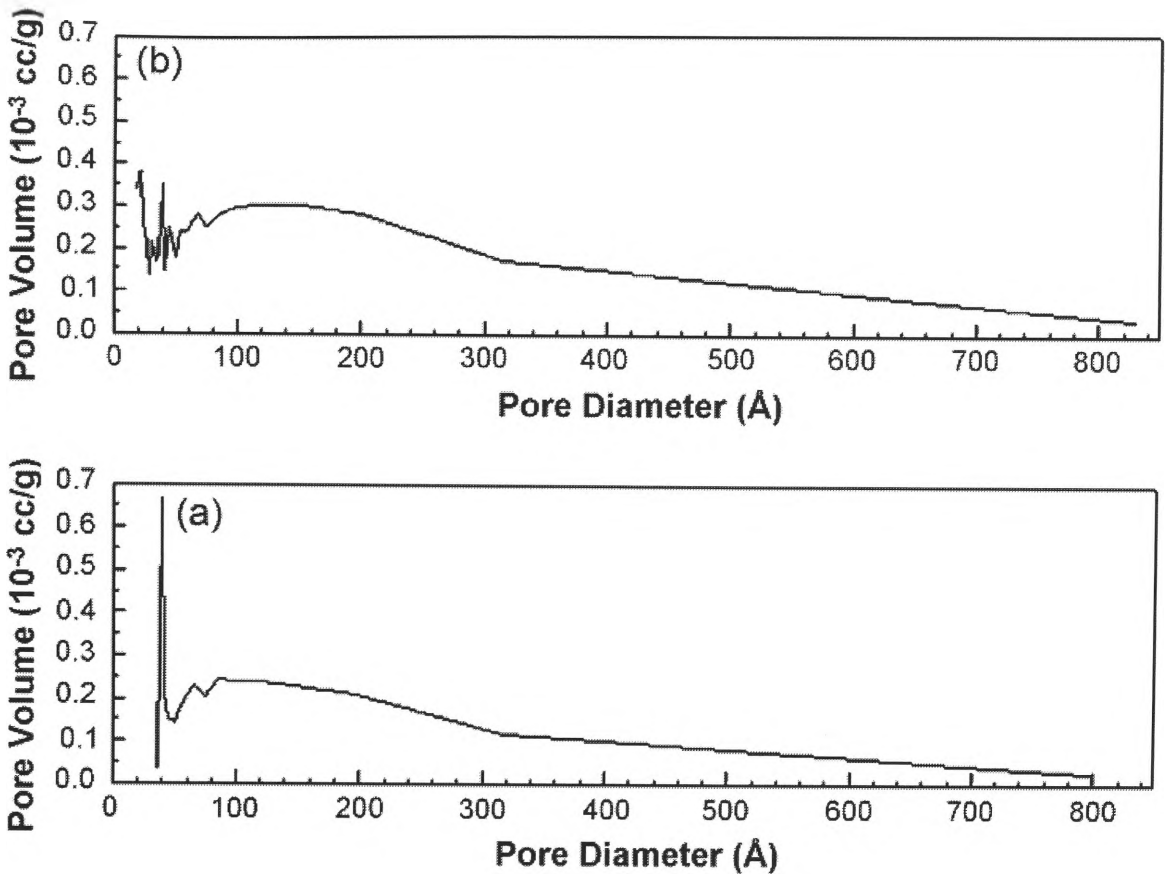

Figure 4-5. Pore size distributions for V_2O_5/carbon composites: (a) obtained at 450 °C; (b) obtained at 500 °C.

4.3.2 Electrochemical Properties

Typical cyclic voltammetric curves of V_2O_5/carbon composite in 2 M KCl at different scan rates are shown in Fig. 4-6. In a previous study [46], it was shown that V_2O_5 yields the highest specific capacitance in a 2-M KCl solution. In Fig. 4-6(a), it can be seen that for V_2O_5/carbon obtained at 450 °C, the CV curve presents a more nearly ideal rectangular shape at a low scan rate (5 mV s^{-1}), compared to the curves at higher scan rates, which proves that there is a constant charging and discharging rate applied over the

specific voltage range [50]. The maximum specific capacitance of 295 F g^{-1} was obtained at a 5-mV s^{-1} scan rate in 2 M KCl solution. The small peaks on the charge and discharge sweeps suggest the insertion and de-insertion of active K^+ ions. Similar CV curves were observed in Fig. 4-6(b) by applying V_2O_5/carbon composite obtained at 500 °C as the electrode active material. The maximum specific capacitance was 233 F g^{-1} in 2 M KCl solution at a 5-mV s^{-1} scan rate.

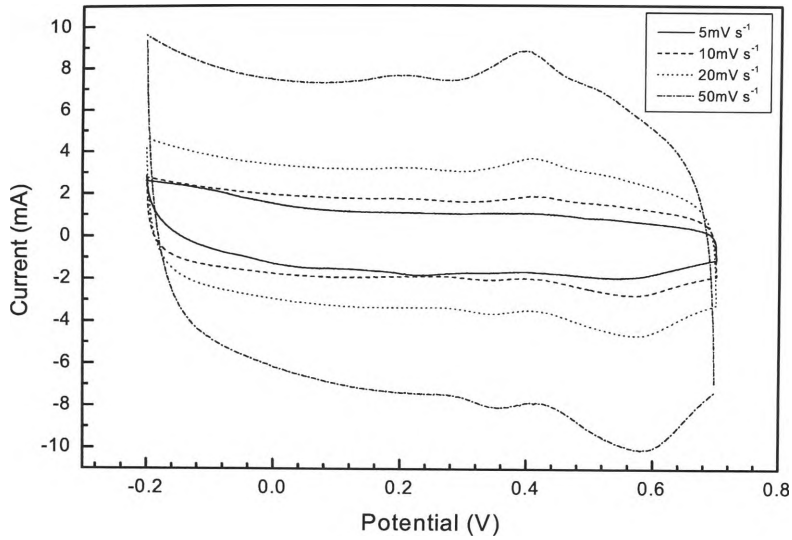

(a)

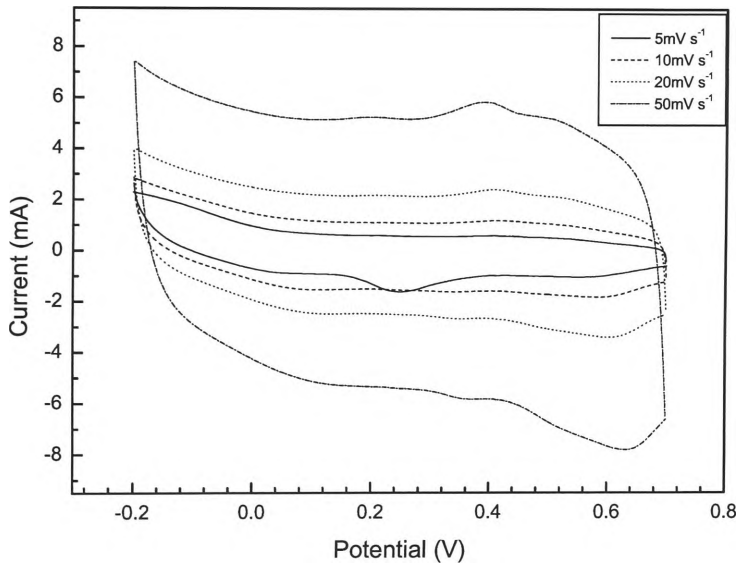

(b)

Figure 4-6. Cyclic voltammetric curves of V_2O_5/carbon sprayed at (a) 450 °C and (b) 500 °C at various scan rates: 5 mV s^{-1}, 10 mV s^{-1}, 20 mV s^{-1}, and 50 mV s^{-1} in 2 M KCl electrolyte.

4.3.3 Discussion

In Table 4-1, the values of the specific capacitance, the specific surface area, and the carbon content for each sample are listed.

Table 4-1. Comparison of specific surface area, specific capacitance values in 2 M KCl at a 5-mV s^{-1} scan rate, and carbon content of the present V_2O_5/carbon materials with those reported in the literature and the previous work.

Electrode active material	Specific surface area (m^2 g^{-1})	Specific capacitance (F g^{-1})	Percentage of carbon-related species (wt%)	Reference
V_2O_5	7	214	0	[45]
V_2O_5	41	262	0	Previous study [46]
V_2O_5/carbon composite	18	295	2.7	Present study at 450 °C
V_2O_5/carbon composite	26	233	1.6	Present study at 500 °C

The data on the first two V_2O_5 materials suggest that V_2O_5 with a higher specific surface area yields a larger specific capacitance. However, for the last two, the V_2O_5/carbon composite materials, the performance is enhanced in the presence of carbon, even with a lower specific surface area. There are a number of reasons that should be taken into account in order to explain these facts. Firstly, the materials are not pure V_2O_5 nanocrystallites, but V_2O_5/carbon composites. The carbon content is a factor that affects both the specific capacitance and the specific surface area. The carbon that is formed in situ in the product increases the electrode conductivity, and contributes to the double-layer specific capacitance, while the nanocrystalline V_2O_5 is responsible for the pseudocapacitance. On the other hand, as has been confirmed by the TEM investigations, the V_2O_5/carbon powders obtained at 450 °C exhibit a specific nanostructure consisting of nanorods and nanoribbons arranged in an open network, which would not be reflected in high values of the specific surface area, but might be more "efficient". This is because it would facilitate contact between the electrolyte and the surface of the material, which is likely to improve ionic diffusion, leading to enhanced electrochemical performance.

At the higher spray temperature (500 °C), the additional carbon oxidation led to an even higher specific surface area in the composite product, but the material has lower conductivity, and the type of porosity is different and possibly not so "efficient" at providing access for the electrolyte to the material surface. The optimal conditions found so far in this study involve spraying the precursor solution at 450 °C to obtain a

V_2O_5/carbon composite product with 2.7 wt% carbon-related species, which yields a high specific capacitance of 295 F g^{-1} in the 2 M KCl electrolyte at a 5-mV s^{-1} scan rate.

4.4 Conclusions

V_2O_5/carbon composite powders were synthesized by spraying the precursor solution in the temperature range of 450-500 °C. Very high capacitance values, up to 295 F g^{-1} in 2 M KCl electrolyte at a 5-mV s^{-1} scan rate, have been measured for V_2O_5/carbon composite powders sprayed at 450 °C. SEM and TEM results revealed a specific unique morphology for this material, which features porous hollow sphere aggregates, with each sphere comprising an open network of nanorods and nanoribbons, with additional nanoribbons protruding from the surfaces. TEM and HRTEM confirmed that this product has V_2O_5 nanocrystalline phase with rod or ribbon sizes ranging from 5 nm to 150 nm and a uniform distribution of amorphous carbon phase. The content of carbon-related species in the composite is 2.7 wt%, as measured by TGA. The BET results showed that the composite powder has a specific surface area of 18 m^2 g^{-1}. The pore size distribution of the sample sprayed at 450 °C indicated a relatively larger pore size, with diameters in the range of 40-50 Å, which would be of benefit for electrochemical performance. The study demonstrates that the presence of carbon in the composite, combined with the specific open network nanostructure can enhance the specific capacitance, and these features are beneficial for the electrochemical performance.

Chapter 5. Cobalt (II, III) Oxide Nanorods as Supercapacitor Electrode Materials

5.1 Introduction

Among various metal oxides, Co_3O_4 is a multifunctional material with promising applications in lithium-ion batteries [51-53], gas sensors [54, 55], electrochromic devices [56], and in catalyst [57, 58] and magnetic materials [59, 60]. Nowadays, nanocrystalline Co_3O_4 is attracting considerable interest for applications in high energy and power density electrochemical capacitors, as it can provide a large surface area and high conductivity, which are two essential properties of a good electrode material. Co_3O_4 electrode also has other significant advantages, such as good efficiency and long-term performance. Its good corrosion stability and low cost make it a promising candidate for supercapacitors [61].

However, few studies have been carried out that consider nanostructured Co_3O_4 as an electrode active material for supercapacitors. Cao et al. reported that they had synthesized mesoporous nanocrystalline Co_3O_4 with high specific capacitance (401 F g^{-1}) and explored it as an active electrode material for supercapacitors [62]. A type of spray-deposited Co_3O_4 film, synthesized on glass substrates by solution spray pyrolysis from aqueous cobalt chloride solution, exhibited a specific capacitance of 74 F g^{-1} [63]. Multi-walled carbon nanotube (MWNT)/Co_3O_4 composite electrode for supercapacitors was prepared through a novel facile and effective method [64]. This MWNT/Co_3O_4 composite showed a specific capacitance of up to 200.98 F g^{-1}, significantly greater than

that of pure MWNTs (90.1 F g^{-1}).

In this chapter, Co_3O_4 nanorods were chemically synthesized through a hydrothermal approach and then characterized by XRD, SEM, and TEM. Pure single phase Co_3O_4 nanocrystals had a flowerlike morphology, as observed by SEM. TEM images showed that the Co_3O_4 nanorods are porous, well aligned, and formed from an aggregation of individual nanocrystals, with an average rod diameter of 150 nm. The specific surface area was determined by the BET technique, and the electrochemical properties were also examined. The maximum specific capacitance was found to be 281 F g^{-1} in 2 M KOH solution at a 5-mV s^{-1} scan rate, which was enhanced by the markedly large specific surface area (232 m^2 g^{-1}). Excellent cycling stability was confirmed, as 83.4% of the specific capacitance was retained after 1000 charge-discharge cycles. It is shown that the as-prepared Co_3O_4 nanorods have potential as a supercapacitor electrode active material.

5.2 Experimental

The synthesis of nanostructured Co_3O_4 was conducted by a hydrothermal method and a further calcination process. The solution was initially prepared by dissolving 6 mmol $CoCl_2 \cdot 6H_2O$ in 20 ml of distilled water and mixing it with 1.5 g of urea under magnetic stirring. Then the mixture was sealed, heated to 110 °C in a Teflon-lined autoclave and maintained at that temperature for 5 h. The precipitate obtained was washed with distilled water, centrifuged several times, and vacuum dried. The resultant precursor was further

heated in an oven (2 °C/min) to 450 °C and kept at 450 °C for another 3 h.

The product was characterized by XRD with a Philips PW 1730 X-ray Generator to identify the phase. The morphology of the Co_3O_4 nanocrystals was examined by a JEOL 6460 model SEM. TEM was performed using a JEOL 2011 200 keV analytical instrument. TEM images were captured at different magnifications to analyze the lattice parameters of the Co_3O_4 nanocystals, as well as the species and the crystal size. The specific surface area of the nanopowders was determined by the gas sorption technique using a Quanta Chrome Nova 1000 Gas Sorption Analyzer based on the BET method.

A beaker-type three-electrode cell was fabricated utilizing Co_3O_4 nanorods with carbon black and PVdF as the working electrode. 63.5 wt% Co_3O_4 nanorods, 27.0 wt% carbon black, and 9.5 wt% PVdF binder were ground thoroughly and dispersed in NMP solvent to form a slurry. Then the slurry was spread onto a piece of platinum foil and maintained at 120 °C in a vacuum oven overnight. Platinum foil and a saturated calomel reference electrode (SCE) were used as the counter electrode and the reference electrode, respectively. The electrochemical properties were evaluated in 2 M KOH electrolyte at room temperature by the CV method on an Electrochemical Workstation (CHI 660C). CV measurements were conducted over a voltage range from –0.25 V to 0.55 V at various scan rates (5 mV s^{-1}, 10 mV s^{-1}, 20 mV s^{-1}, 50 mV s^{-1}, and 100 mV s^{-1}). Cycling tests were performed in the same voltage range, with a scan rate of 100 mV s^{-1} for 1000 charge-discharge cycles.

5.3 Results and Discussion

5.3.1 Characterizations

As shown in Fig. 5-1, all the peaks in the XRD pattern can be indexed to spinel structured Co_3O_4 (PDF card 42-1467) in the diffraction database, which means that a pure single, well-crystallized Co_3O_4 phase was confirmed in the range of 2θ from 15 ° to 70 °. The average crystal size of the Co_3O_4 crystallites was evaluated by the well-known Scherrer formula and found to be about 140 nm.

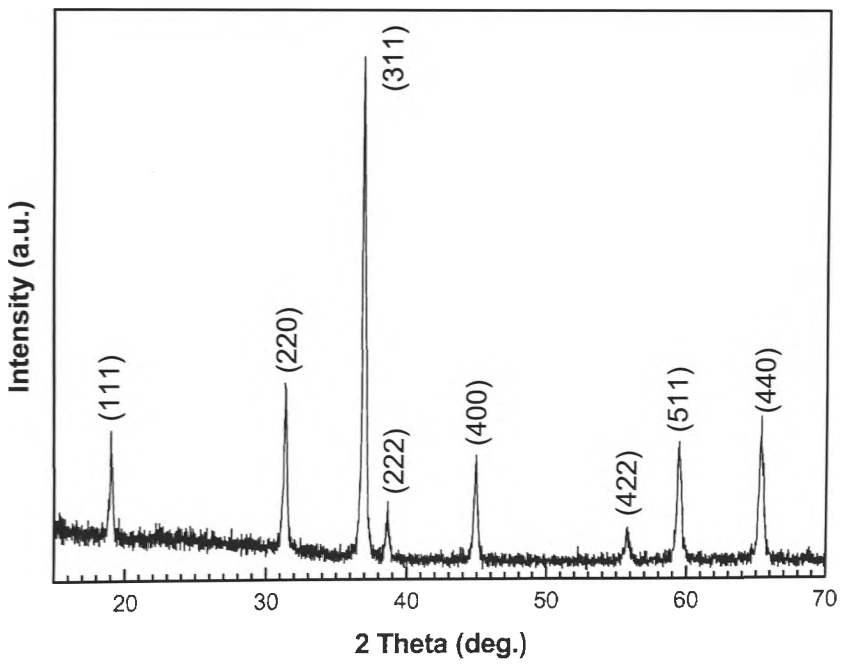

Figure 5-1. X-ray diffraction pattern of the as-prepared Co_3O_4 nanorods.

A typical SEM image (Fig. 5-2(a)) clearly shows that the as-prepared Co_3O_4 nanocrystals have a unique flowerlike morphology. These flowerlike aggregations consist of highly ordered rods, which were extended from the "root" (Fig. 5-2(b)). The rods were evaluated to have nanometer dimensions.

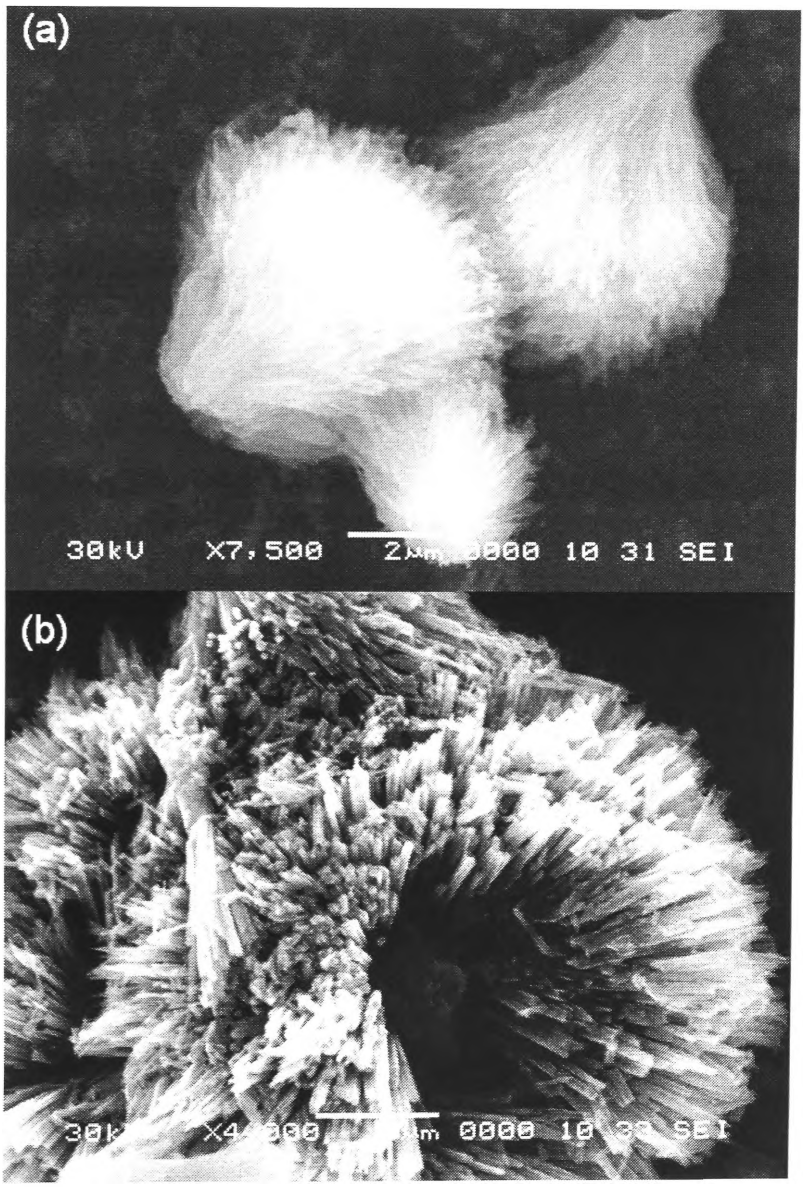

Figure 5-2. SEM images of the as-prepared Co_3O_4 nanorods at different magnifications: (a) flowerlike aggregations; (b) highly ordered nanorods.

The TEM image in Fig. 5-3(a) displays the as-prepared Co_3O_4 resulting from the hydrothermal method. The morphologies of Co_3O_4 are short nanorods with an average diameter of 150 nm and lengths of a few micrometers. In this low magnification view, the nanorods were found to have a porous structure, being composed of agglomerates of nanoparticles. Fig. 5-3(b) shows the large area electron diffraction pattern of randomly oriented nanorods. The distance from the direct beam spot in the middle to each ring corresponded to the d-spacing of each ring indexed to the planes (1 1 1), (2 2 0), (3 1 1), and (4 0 0) from the inner ring, respectively, and matched to the Co_3O_4 characteristic planes, as shown in XRD.

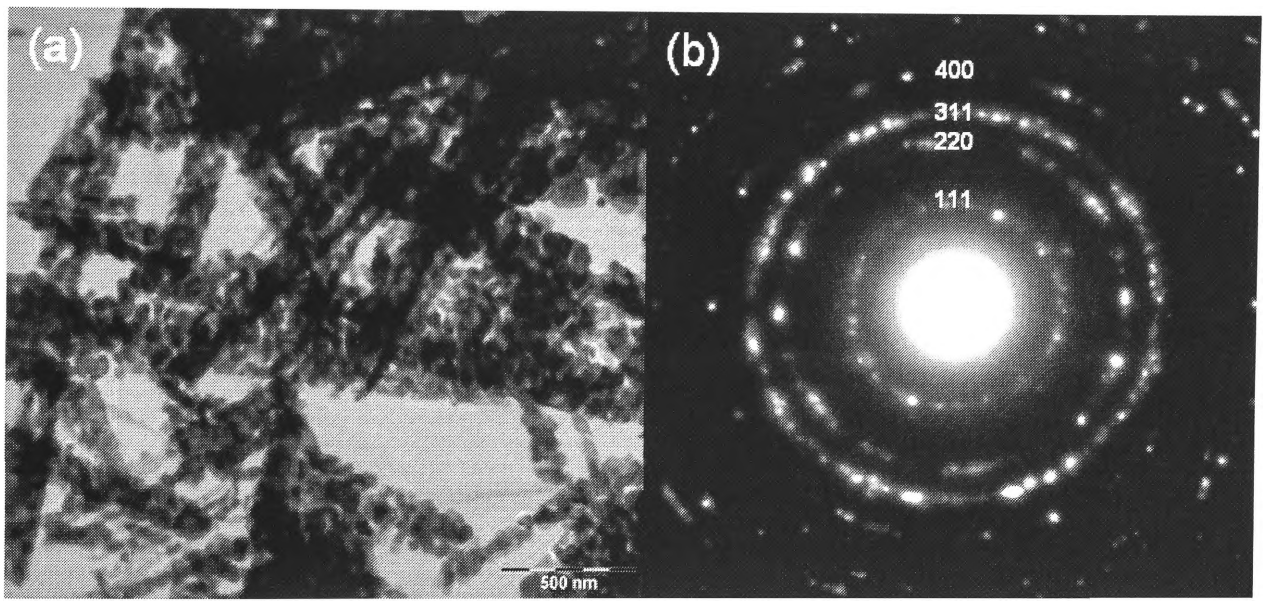

Figure 5-3. TEM images of the as-prepared Co_3O_4 nanorods: (a) at a low magnification; (b) large area electron diffraction pattern.

The fringe of a Co_3O_4 nanorod was observed on the atomic scale by High Resolution TEM (HRTEM) in Fig. 5-4(a). The interplanar spacing was measured to be 0.285 nm,

which was matched to the d-spacing of the (2 2 0) planes. The low magnification observations aroused suspicion about the structure of Co_3O_4, suggesting that the nanorods are aggregates of small nanoparticles. Further investigation was conducted by Selected Area Electron Diffraction (SAED). The SAED pattern in Fig. 5-4(b) was taken at the [0 0 1] zone axis. All spot indices are denoted on the pattern image. From the SAED, no spots were observed that were derived from another crystal. This confirmation supported the view that the nanorods grew in one direction in accordance with one another during the synthetic process. This result provided solid evidence to add to the HRTEM image observations, and the Co_3O_4 nanorods were confirmed to consist of single nanocrystals with many pores (Fig. 5-4(c)).

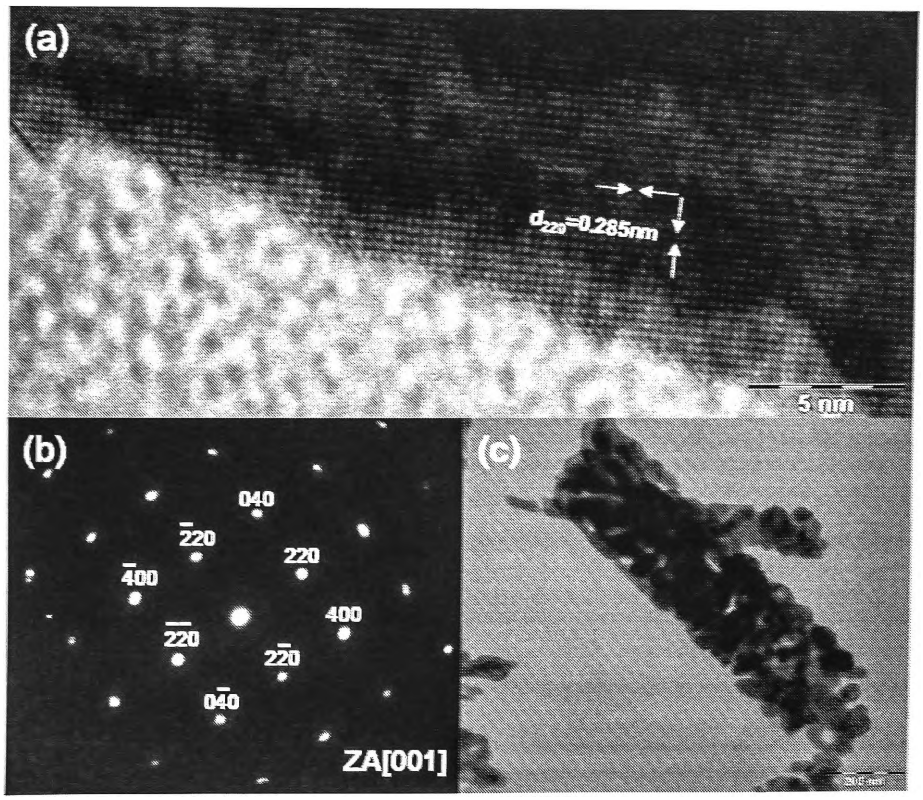

Figure 5-4. TEM images of the as-prepared Co_3O_4 nanorods: (a) HRTEM image on the atomic scale; (b) SAED pattern; (c) HRTEM image at a high magnification.

BET measurements proved that the as-prepared Co_3O_4 nanorods have an extremely large value for their specific surface area, 232 $m^2 g^{-1}$, compared to 7 $m^2 g^{-1}$ for the commercial Co_3O_4 powders. The porosity was considered to be the major contributor to the large specific surface area.

5.3.2 Electrochemical Properties

Typical cyclic voltammograms of Co_3O_4 nanorods in 2 M KOH at different scan rates are shown in Fig. 5-5. All the CV curves at varied sweep rates presented similar shapes with obvious redox peaks rather than ideally rectangular shapes. This indicates that the specific capacitance obtained is not pure double-layer capacitance, but mainly based on faradaic pseudocapacitance. The maximum specific capacitance of 281 F g^{-1} was obtained at a 5-mV s^{-1} scan rate in 2 M KOH solution. Commercial Co_3O_4 powders were also tested through the same procedures for comparison, giving a maximum specific capacitance value of 43 F g^{-1}.

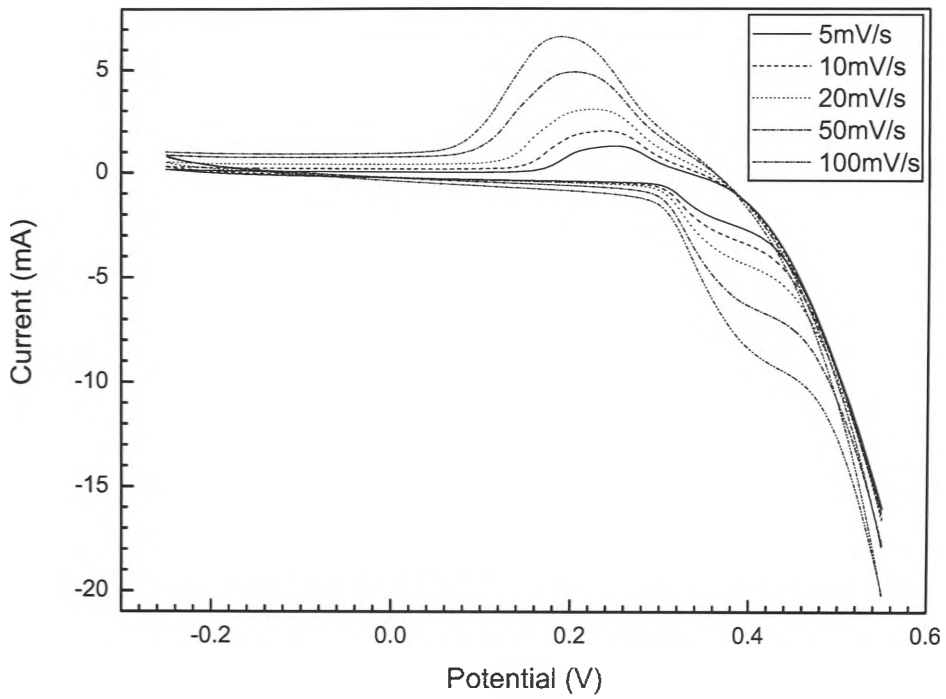

Figure 5-5. Cyclic voltammetric curves of the as-prepared Co_3O_4 nanorods at various scan rates: 5 mV s^{-1}, 10 mV s^{-1}, 20 mV s^{-1}, 50 mV s^{-1}, and 100 mV s^{-1} in 2 M KOH electrolyte.

Cycling tests of the Co_3O_4 nanorods compared the first and the 1000th cycle of CV curves (Fig. 5-6), and it was revealed from the computation that 83.4% of the specific capacitance remained after 1000 charge-discharge cycles using an open cell test.

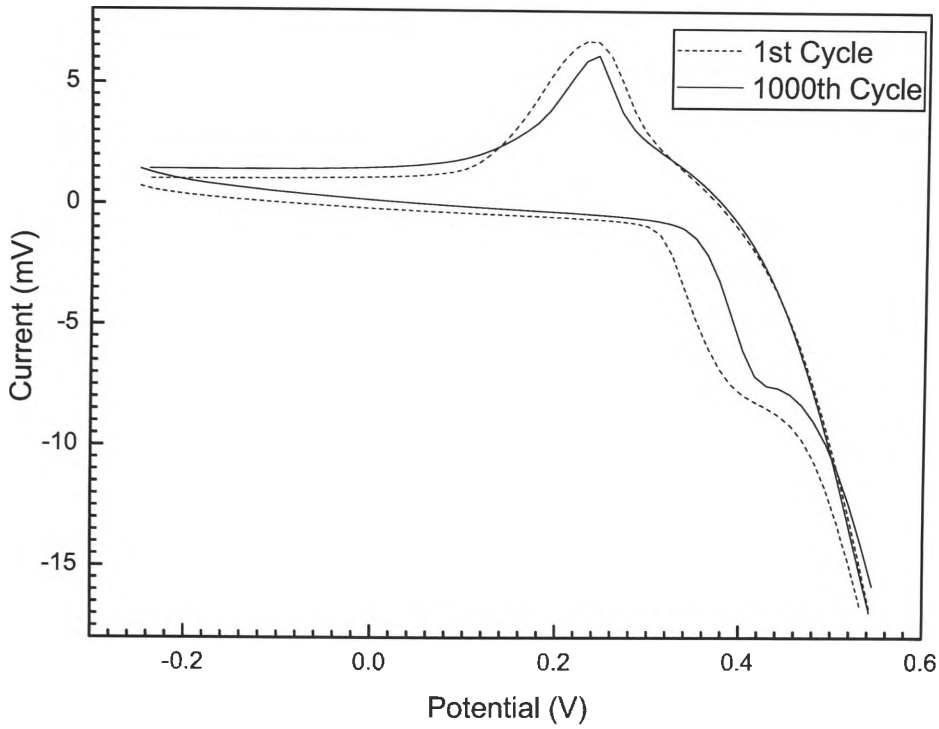

Figure 5-6. 1st and 1000th charge-discharge cyclic voltammograms of the as-prepared Co_3O_4 nanorods at a 100-mV s^{-1} scan rate in 2 M KOH electrolyte.

5.3.3 Discussion

In this study, Co_3O_4 nanorods exhibited a very much larger specific capacitance than that of commercial Co_3O_4 powders, due to the larger specific surface area of the highly ordered nanorods. Nanocrystalline Co_3O_4 also offers electrochemical stability, high

conductivity, and pseudocapacitive behavior, which make a significant contribution to the specific capacitance as well, thus enhancing the electrochemical properties.

5.4 Conclusions

Pure, single phase Co_3O_4 polycrystalline nanorods were prepared through a facile chemical route and characterized by XRD, SEM, TEM and BET. Nanocrystalline Co_3O_4 formed flowerlike aggregations consisting of highly ordered rods. The rods consist of single Co_3O_4 nanocrystals and have a porous structure. The high specific surface area, 232 m^2 g^{-1}, would be of benefit for the electrochemical performance. The as-prepared Co_3O_4 nanorods yielded a maximum specific capacitance of 281 F g^{-1} with excellent cycling stability, which reveals its potential to be used as a supercapacitor electrode material.

Chapter 6. α-Iron (III) Oxide Nanorods for Supercapacitor Application

6.1 Introduction

Iron oxides, especially Fe_3O_4, are attractive due to their low cost and large specific surface area. The highest reported specific capacitance of Fe_3O_4 was 510 F g^{-1}, achieved with a Fe_3O_4-carbon black composite [65]. γ-Fe_2O_3 films were prepared by cathodic electrosynthesis and yielded a maximum specific capacitance of 210 F g^{-1} in 0.025 M $Na_2S_2O_3$ solution, at a scan rate of 2 mV s^{-1} [66].

Among all the iron oxides, hematite Fe_2O_3 (α-Fe_2O_3) is the most stable compound, formed by hexagonal close packed oxygen atoms together with iron atoms, in a 2:3 ratio to the oxygen atoms, occupying the octahedral vacancies [67]. As nanosized α-Fe_2O_3 has better electrochemical performance than micron-sized α-Fe_2O_3 [68–70], it is widely considered as a potential electrode material for electrochemical devices, such as lithium-ion batteries. The synthesis of hematite Fe_2O_3 nanocrystals has been studied intensively. Various preparation methods, such as template [71], sol–gel [72], gas–solid reactions [73], and hydrothermal techniques [74, 75], have been developed to synthesize hematite Fe_2O_3 nanostructures with controllable size and shape [76]. α-Fe_2O_3 with different morphologies, nanorods [72], nanotubes [74], nanocrystals [77], nanoparticles [78], nanocuboids [79], nanospindles [80], nanoflakes [81], nanowires [82], and nanobelts [83], has been successfully prepared through the above techniques.

The synthesis of α-Fe_2O_3 nanorods is reported here, through a hydrothermal route, which provides convenient homogeneous nucleation and grain growth [84]. Characterizations by XRD, SEM, and TEM are also reported. TEM analysis revealed the formation of Fe_2O_3 nanorods, growing in pairs with pores in the middle. These were composed of pure hematite Fe_2O_3 phase, and the nanorods had diameters less than 100 nm. The electrochemical properties of the α-Fe_2O_3 rods, with a specific surface area of 81 $m^2 g^{-1}$, were investigated to determine the possibilities of their being used as a supercapacitor electrode material. A beaker-type three-electrode cell was fabricated and tested in 2 M $Na_2S_2O_3$ solution. The as-prepared product yielded a specific capacitance of up to 72 F g^{-1} at a 5-mV s^{-1} scan rate.

6.2 Experimental

α-Iron (III) oxide (Fe_2O_3) nanorods were prepared by the hydrothermal method. 2 mmol of commercial $FeCl_3$ powders, 30 ml of distilled water, and 5 mmol of urea were mixed thoroughly under magnetic stirring, then transferred to a Teflon-lined autoclave heated in an oven to 120 °C and maintained at that temperature for 10 h. The resultant precipitate was washed and centrifuged several times to remove any soluble ions. Afterwards, the precipitate was vacuum dried at 60 °C overnight.

The as-prepared powders were characterized by XRD with a GBC MMA X-ray

diffraction unit to identify the phase. A JEOL 6460 model SEM was used to examine the morphology of the Fe_2O_3 nanocrystals. TEM images were captured by a JEOL 2011 200 keV analytical instrument at different magnifications to analyze the lattice parameters of the Fe_2O_3 nanocystals, as well as the species and the crystal size. BET measurements based on the gas sorption technique were performed on a Quanta Chrome Nova 1000 Gas Sorption Analyzer to determine the specific surface area of the nanopowders.

CV tests were carried out on an Electrochemical Workstation (CHI 660C) to investigate the electrochemical properties of the Fe_2O_3 nanorods. The working electrode was made by dispersing 65.5 wt% as-prepared Fe_2O_3 nanorods, 27.5 wt% carbon black, and 7 wt% PVdF in NMP. A piece of platinum foil and a saturated calomel reference electrode (SCE) were used as the counter electrode and the reference electrode, respectively. A beaker-type three-electrode cell was fabricated using the above electrodes, with 2 M $Na_2S_2O_3$ solution as the electrolyte. CV tests were conducted over a voltage range from –0.9 V to -0.1 V at various scan rates (5 mV s^{-1}, 10 mV s^{-1}, 20 mV s^{-1}, 50 mV s^{-1}, and 100 mV s^{-1}) to compute the specific capacitance.

6.3 Results and Discussion

6.3.1 Characterizations

Fig. 6-1 shows the XRD pattern of the as-synthesized product with 2θ ranging from 15 °

to 60 °. The characteristic peaks are consistent with the hematite Fe_2O_3 (α-Fe_2O_3) phase, which was confirmed by PDF card 24-0072. The average crystal size of the Fe_2O_3 crystallites was found to be about 60 nm, as evaluated by the Scherrer formula.

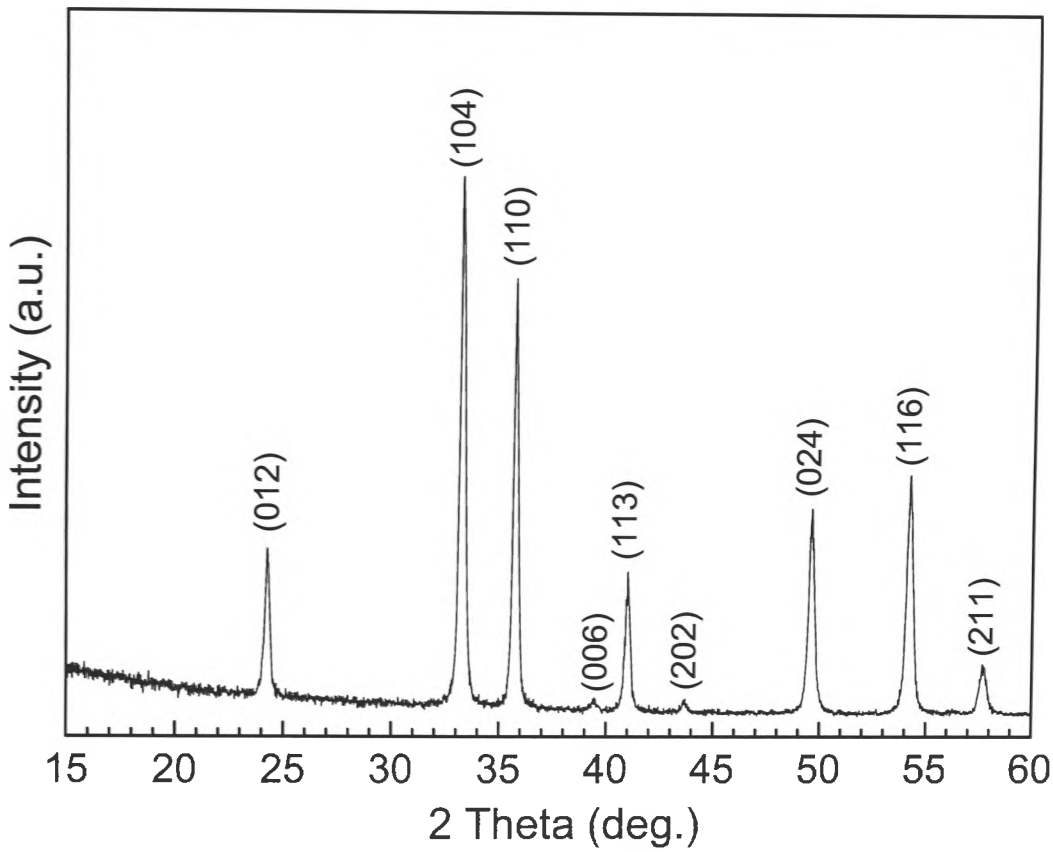

Figure 6-1. X-ray diffraction pattern of the as-prepared Fe_2O_3 nanorods.

SEM images, as shown in Fig. 6-2, captured at 30,000× magnification, present a morphology with the nanorods firmly joined to each other, with an average rod diameter less than 100 nm.

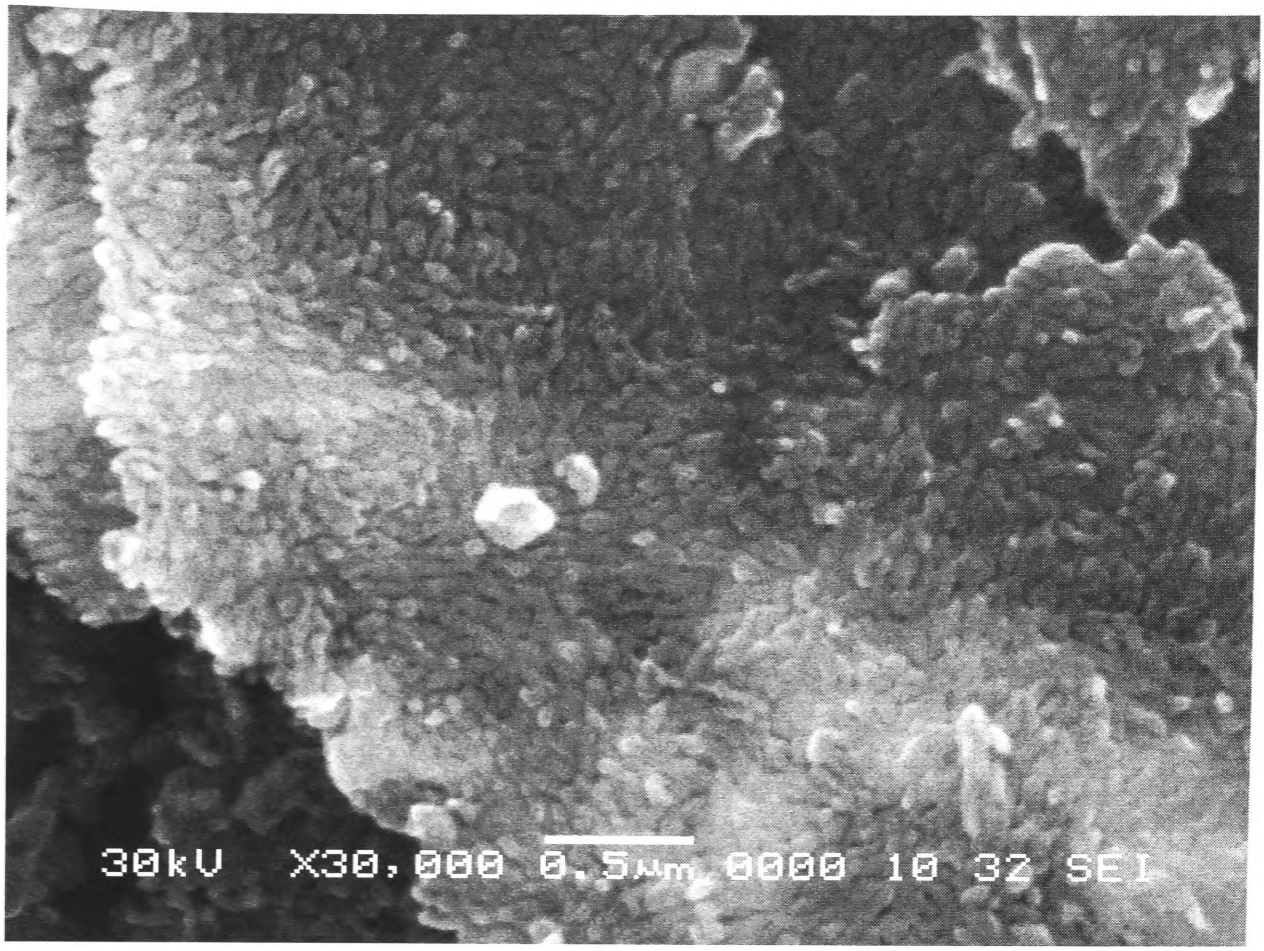

Figure 6-2. SEM image of the as-prepared Fe_2O_3 nanorods captured at 30,000× magnification.

The TEM image shown in Fig. 6-3 displays the interesting structure of the Fe_2O_3 nanorods synthesized by the hydrothermal method. The individual nanorods grew in a parallel direction and formed thick junctions, so that two rods combined and accommodated pores in the middle. The diameters of the nanorods were evaluated to be in the range of 20–60 nm.

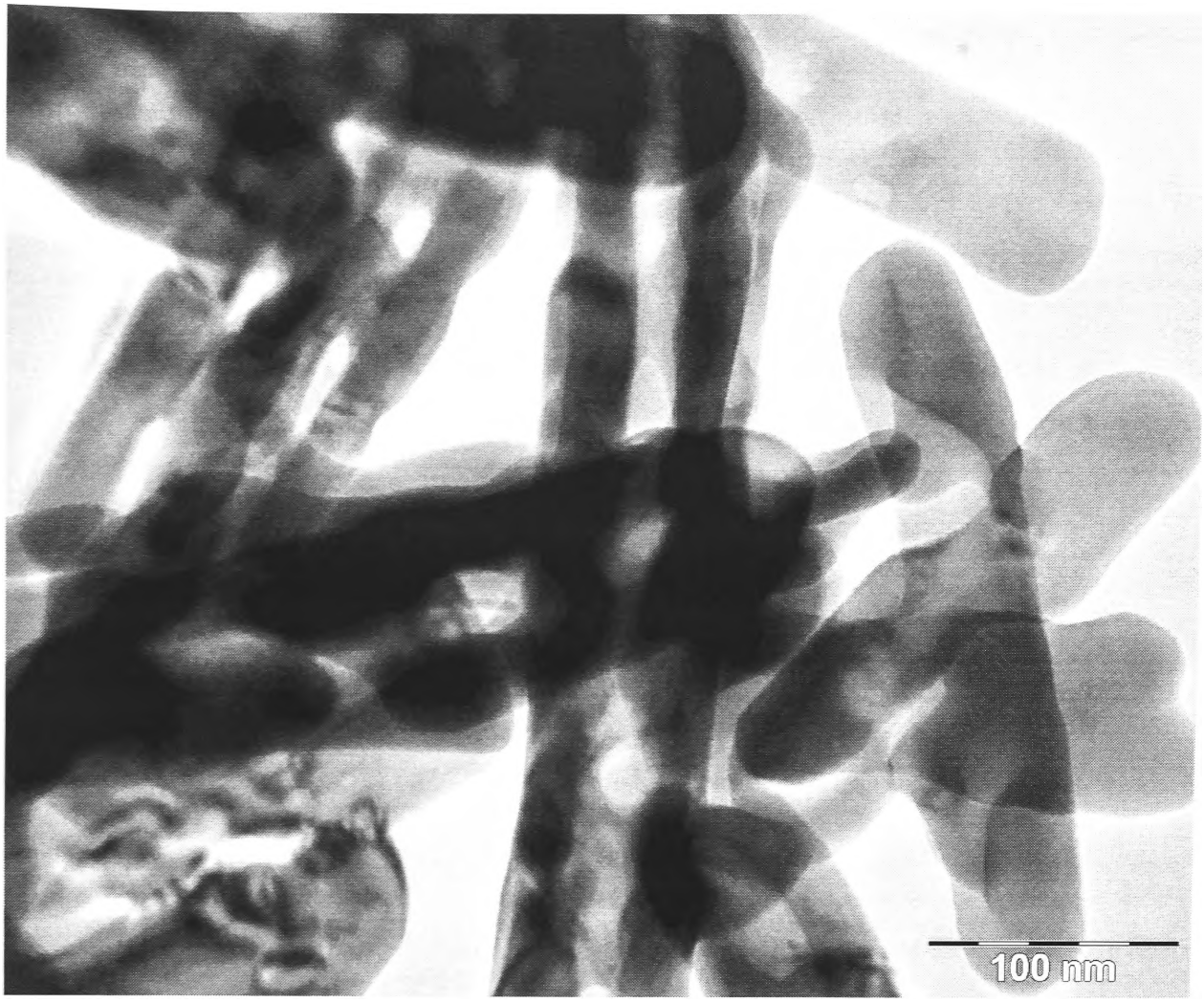

Figure 6-3. TEM image of the as-prepared Fe_2O_3 nanorods at low magnification.

A High Resolution TEM (HRTEM) image of a selected area at the tip of a nanorod is shown in Fig. 6-4 and its corresponding diffraction pattern appears in the inset. The image clearly shows paired, well aligned nanorod growth. As seen in Fig. 6-4, the interplanar spacing is 0.27 nm over the whole area observed from one rod to another at the fringe of two rods. This d-spacing is the same as for the (1 0 4) planes. This is confirmed by the Selected Area Electron Diffraction (SAED) pattern in the inset of Fig. 6-4. Many nanorods grew in pairs, and this would come from the preference to reduce

the surface energy during the synthetic process. Morphology modified, as well as as-prepared Fe_2O_3 nanorods might be obtained by parameter control.

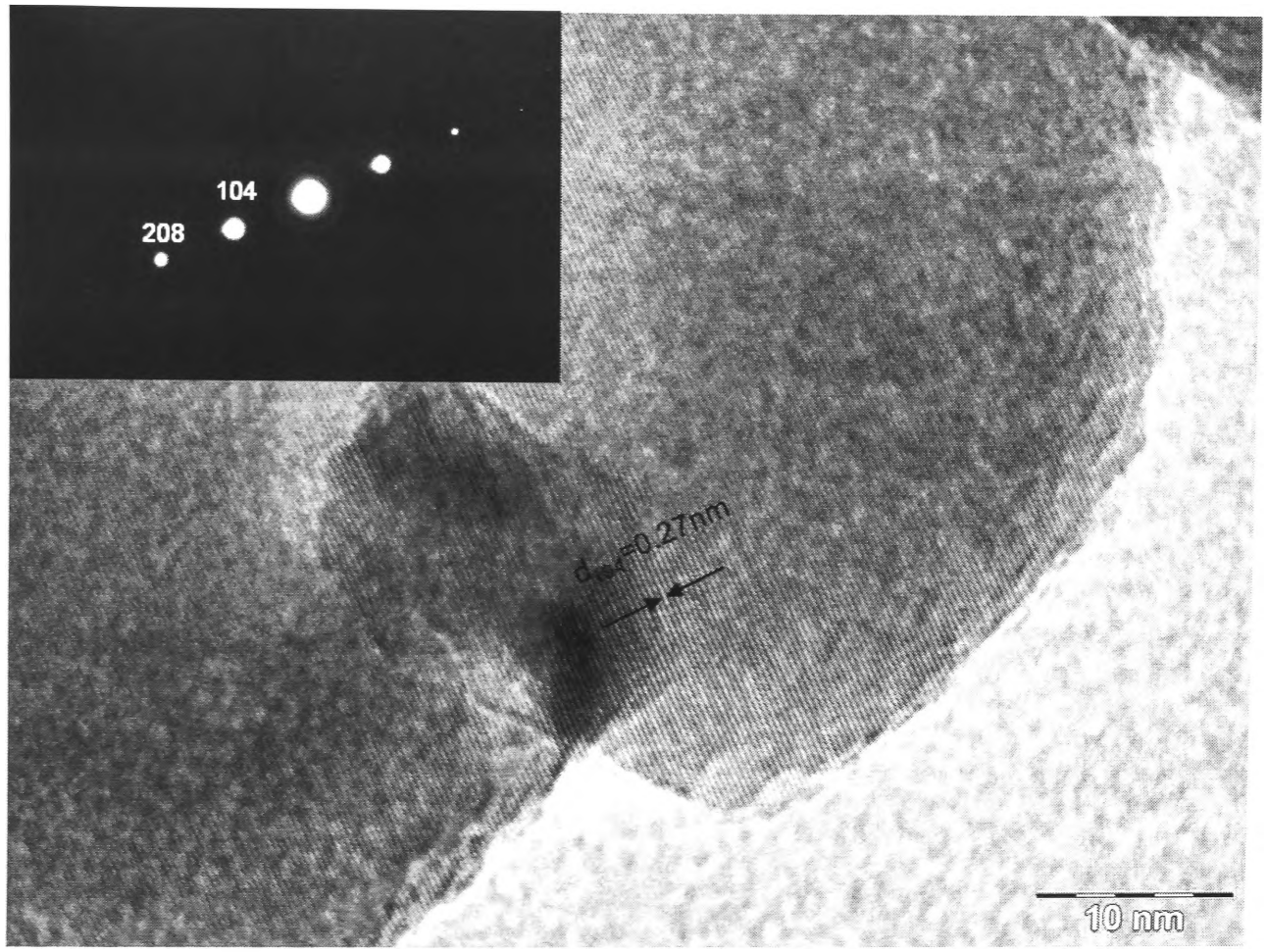

Figure 6-4. HRTEM image of the tip of a Fe_2O_3 nanorod. The inset shows the corresponding SAED pattern.

6.3.2 Electrochemical Properties

Electrochemical testing was initially applied to commercial Fe_2O_3 in various electrolytes, and it was found that 2 M $Na_2S_2O_3$ solution is the most suitable electrolyte, in which commercial Fe_2O_3 yields the highest specific capacitance, 10 F g^{-1}, over the entire

voltage range. The typical CV curves of the as-prepared Fe_2O_3 nanorods at different scan rates are shown in Fig. 6-5. It can be seen that the CV curve obtained at 5 mV s^{-1} presents a more nearly ideal rectangular shape compared to the curves at higher scan rates, which implies a constant charging and discharging rate over the voltage range [50]. The shape of the CV curves showed that it is double-layer capacitance that mainly contributes to the maximum specific capacitance, 72 F g^{-1}, achieved at a 5-mV s^{-1} scan rate in 2 M $Na_2S_2O_3$ solution.

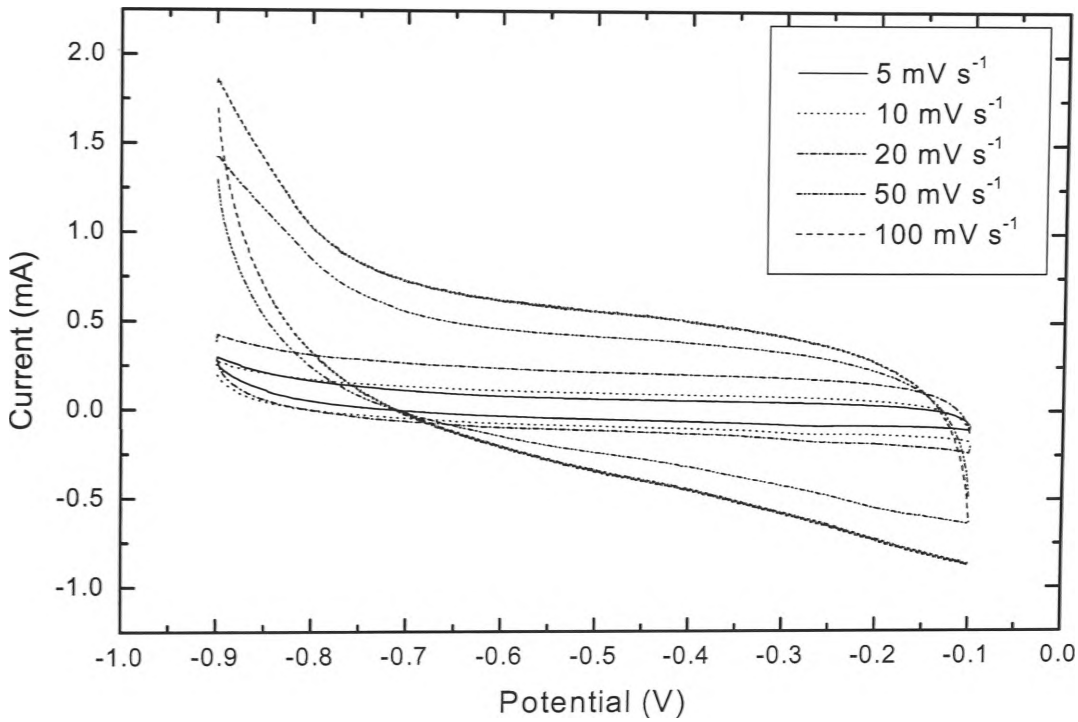

Figure 6-5. CV curves of the as-prepared Fe_2O_3 nanorods at various scan rates: 5 mV s^{-1}, 10 mV s^{-1}, 20 mV s^{-1}, 50 mV s^{-1}, and 100 mV s^{-1} in 2 M $Na_2S_2O_3$ electrolyte.

6.3.3 Discussion

The electrochemical performance of the active material is related to the specific surface area. BET measurements revealed that the as-prepared Fe_2O_3 nanorods have a relatively larger specific surface area, 81 m^2 g^{-1}, compared to that of the commercial Fe_2O_3 powders (19 m^2 g^{-1}). The morphology of the nanorods makes an extra contribution to the specific surface area, which would provide sufficient surface interactions to allow the insertion and de-insertion of the active ions through the working electrode, thus enhancing the specific capacitance. α-Fe_2O_3 nanorod based working electrode exhibited acceptable supercapacitive properties during the electrochemical analysis, implying that it is suitable for electrochemical supercapacitor applications.

6.4 Conclusions

α-Fe_2O_3 nanorods were synthesized by the hydrothermal method from commercial $FeCl_3$ and urea. The product was characterized and tested for use as a supercapacitor electrode material. Nanorods of Fe_2O_3 with diameters in the range of 20–60 nm were joined together, forming well-crystallized structures. The growth of the nanorods was deduced to reduce the surface energy, as the majority of the rods were joined into pairs during the synthetic process. The maximum value of the specific capacitance, 72 F g^{-1}, was obtained from the α-Fe_2O_3 nanorods at a 5-mV s^{-1} scan rate in 2 M $Na_2S_2O_3$ electrolyte. The electrochemical performance is considered to be affected by the morphology and the

specific surface area of this electrode material. In this study, the high specific surface area offered by the nanorods plays an important role in helping to improve the electrochemical properties.

Chapter 7. Examinations of Other Metal Oxides as Supercapacitor Electrode Materials

In this chapter, several materials were examined as supercapacitor electrode materials. A brief explanation of each examination is presented.

7.1 V_2O_5 by Precipitation

The synthesis of nanostructured V_2O_5 powders was conducted by co-precipitation and further calcination, which were simple and easily handled. 0.2 M vanadium trichloride (VCl_3) aqueous solution and 0.2 M ammonium hydroxide ($NH_3 \cdot H_2O$) aqueous solution were prepared prior to co-precipitation. The ammonium hydroxide was added dropwise to the vanadium trichloride solution under rigorous magnetic stirring. After the reaction, the resultant precipitate was centrifuged and washed several times with distilled water to remove any soluble products. The precipitate was dried in a vacuum oven at 80 °C overnight and then heated in an open furnace at 250 °C for 1.5 h.

The characteristic CV curves are shown in Fig. 7-1. At each scan rate, the ideal rectangular shape is displayed. The nanostructured V_2O_5 yielded a maximum specific capacitance of 267 F g^{-1} in 2 M KCl solution at a scan rate of 5 mV s^{-1}. Compared to the V_2O_5/carbon composite material in Chapter 4, the specific capacitance is smaller, due to the smaller BET specific surface area, 10 m^2 g^{-1}, and the lack of micropores in the morphology.

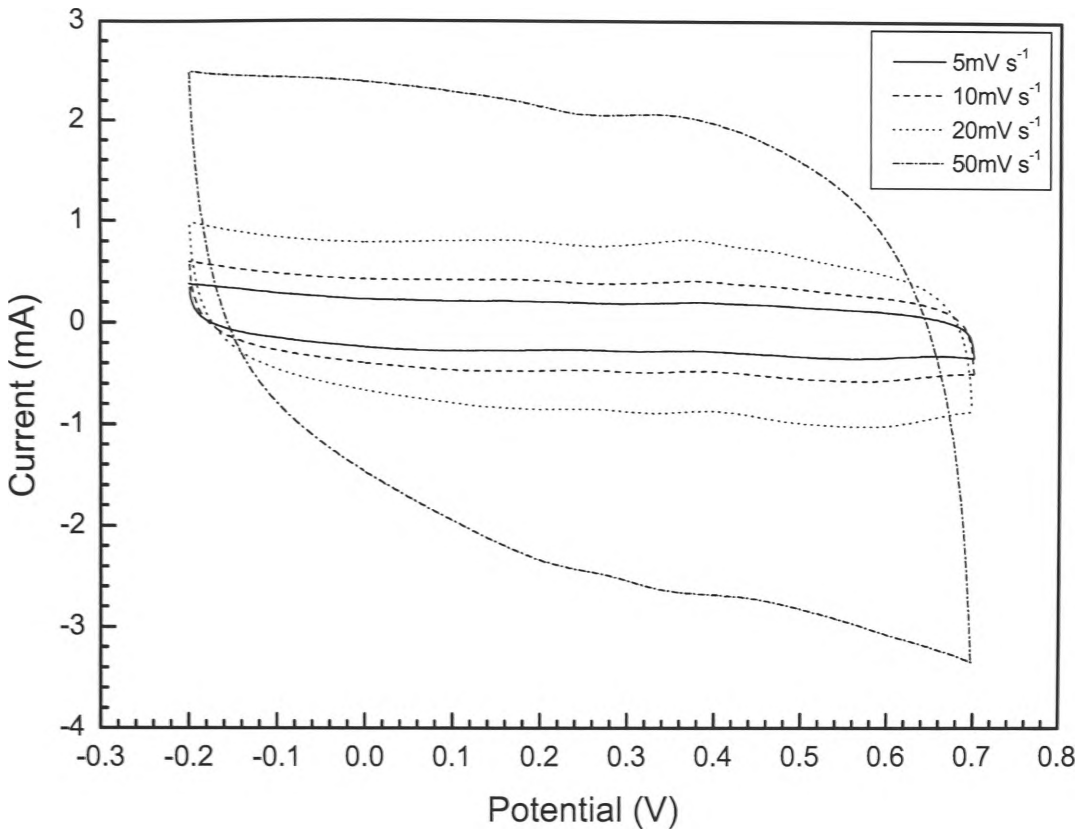

Figure 7-1. CV curves of as-prepared V_2O_5 in 2 M KCl solution at various scan rates: 5 mV s^{-1}, 10 mV s^{-1}, 20 mV s^{-1}, and 50 mV s^{-1}.

7.2 VO_2 by Precipitation

Thermochromic rutile-type vanadium dioxide (VO_2) is attracting considerable interest, as it has many potential applications such as optical switching and detection [85, 86], optical storage [87], laser protection [88], smart window coatings [89], etc. All these applications are based on the principle that VO_2 undergoes an abrupt semiconductor-metal transition near 68 °C, accompanied by a crystallographic transition from a monoclinic low-temperature phase to a tetragonal high-temperature phase [90], which leads to dramatic changes in electrical and optical properties. The transition results in a change in electrical resistivity by up to 105 times for VO_2, as well as dramatic variation of infrared transmission characteristics.

Nanostructured VO_2 films have been prepared on amorphous SiO_2/Si substrates [91], and sol-gel derived VO_2 thin films were obtained by deposition of vanadium alkoxide molecular precursors onto a fused silica substrate using the spin coating technique [92]. Later, nanorods of B phase VO_2 with high crystallinity and high surface area were synthesized by the hydrothermal method using an organic surfactant [93]. Metastable VO_2 nanowire arrays were prepared by an ethylene glycol reduction approach [94]. Furthermore, with NH_4NO_3 as the source of vanadium and formic acid as the reducing and acidifying agent, VO_2 nanorods can be synthesized by the hydrothermal method [95]. It was reported by Sediri et al. that the synthesis of nano-needle VO_2 (B) from foam could be successful when using the crystalline V_2O_5 as the starting precursor and aniline

as the reducing agent [96]. Sediri et al. later demonstrated another approach using V_2O_5 as the source of vanadium and benzylamine as the reducing agent for the preparation of vanadium dioxide nanorods [97].

The synthesis of VO_2 followed the same procedures as stated in the last subsection for V_2O_5 made by precipitation, except that the precipitates were then heated in a furnace at 250 $^{\circ}C$ under flowing gas (10% H_2 in Argon) for another 2 h. Afterwards, the powders were cooled slowly to room temperature and collected for characterization.

The specific capacitance of VO_2 nanopowders is not high, with the highest value 50-60 F g^{-1} in 1 M KCl and 70-80 F g^{-1} in 2 M KCl respectively, at a scan rate of 5 mV s^{-1}. The low capacitance might due to the low specific surface area, which is less than 3 m^2 g^{-1}. In this case, VO_2 is not a suitable candidate for supercapacitor applications.

7.3 V_2O_5 Thin Film via Dip-coating

Dip-coating is a versatile tool, which coats thin films onto complex substrate geometries at low capital and operational costs on the industrial scale. Thin films theoretically can hold a greater energy/power density, due to the high surface area/volume ratio, when compared to bulk prepared materials. The increased energy density allows supercapacitors and batteries to be reduced in size whilst still containing the energy of a larger bulk cell. A thin film also provides many contact points between the active material and the collector electrode due to good adhesion, and the availability of many conductive pathways for electrons to the collector foil lowers the internal resistance.

The spontaneous growth of V_2O_5 nanorods was observed to occur from dip-coating with a 0.2 M precursor solution (the same precursor solution prepared in Chapter 4). Cyclic voltammetry curves of V_2O_5 thin film on platinum are not in the ideal rectangular shape, as shown in Fig. 7-2, where there are obvious redox peaks. This means that pseudocapacitance contributes to the specific capacitance. The largest specific capacitance was determined to be 88-94 F g^{-1}, obtained in 2 M KCl solution at 5 mV s^{-1}.

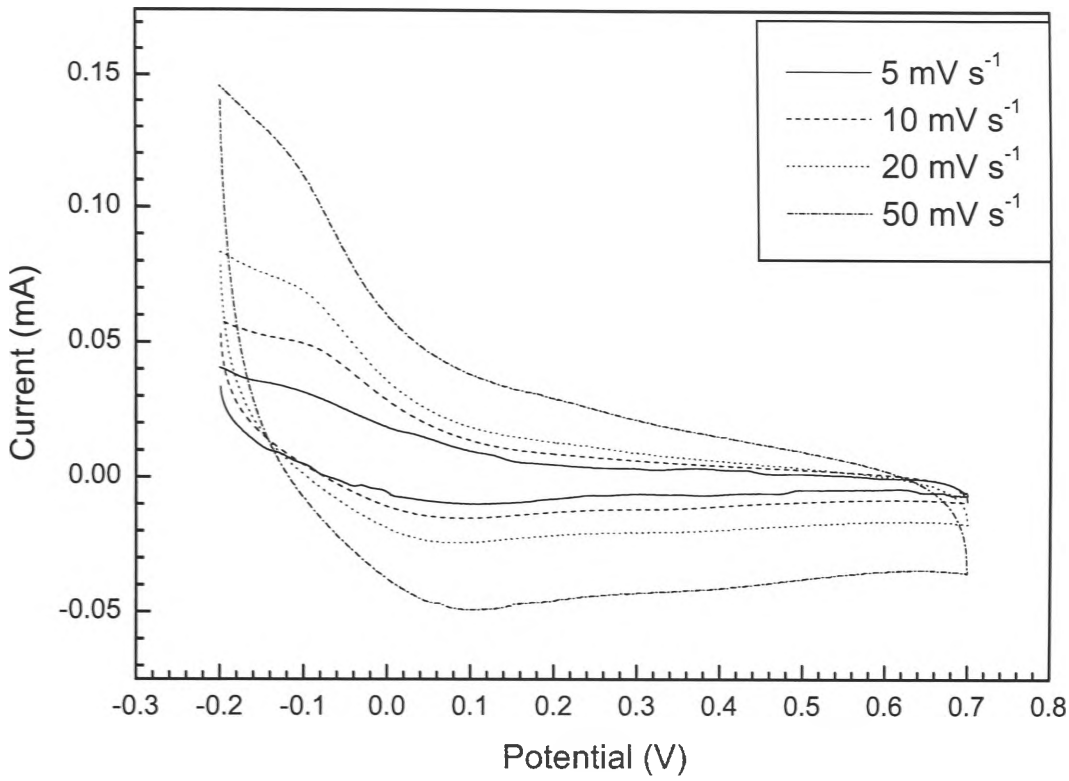

Figure 7-2. CV curves of the as-prepared V_2O_5 thin film at various scan rates: 5 mV s^{-1}, 10 mV s^{-1}, 20 mV s^{-1}, and 50 mV s^{-1} in 2 M KCl electrolyte.

7.4 Carbon Coated Fe_2O_3 Nanorods

The precursor α-iron (III) oxide (Fe_2O_3) nanorods were initially synthesized by the hydrothermal method (detailed in Chapter 6). Then, the Fe_2O_3 nanorods were added into a solution which was made by dissolving citric acid (weight ratio, Fe_2O_3: citric acid = 1: 2) in 5 ml ethanol, and the mixture was kept under magnetic stirring for 24 h. After stirring and evaporation, a gel was formed and dried in a vacuum oven. The resultant powders were heated in a furnace at 300 °C for 2 h under an Ar/O_2 (95%/5%) atmosphere.

The XRD peaks show that the coated product contains a mixed phase with Fe_2O_3 and Fe_3O_4. Amorphous carbon is also present, but not shown on the XRD. The maximum specific capacitance was 71 F g^{-1}, achieved at a 5-mV s^{-1} scan rate in 2 M $Na_2S_2O_3$ solution.

The coating would be expected to enhance the electrochemical properties of Fe_2O_3 nanorods, as carbon composite electrode will have adequate electronic conductivity, hence increase the specific capacitance. However, the specific capacitance is 71 F g^{-1} based on the CV measurements, without much improvement compared to the non-coated Fe_2O_3 nanorods. The BET result, 16 m^2 g^{-1}, confirms that the low performance is owing to the small specific surface area of the coated product.

7.5 Fe_3O_4 by Spray Pyrolysis

Fe_3O_4 nanopowders were synthesized by spray pyrolysis. The product exhibited non-ideal CV curves with redox peaks. The typical CV curve (Fig. 7-3) was obtained in 1 M Na_2SO_3 solution at a scan rate of 5 mV s^{-1}. The specific capacitance was estimated to be 167 F g^{-1}, larger than most of the specific capacitance values in the literature.

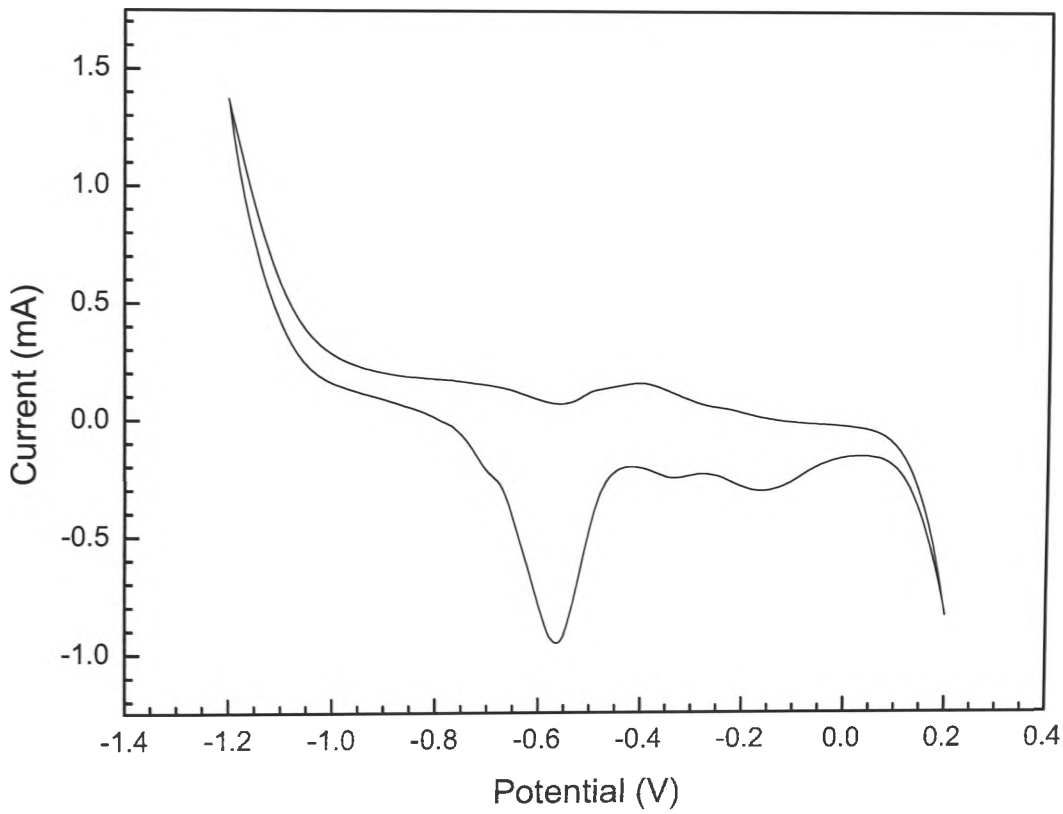

Figure 7-3. CV curve of the as-prepared Fe_3O_4 at a scan rate of 5 mV s^{-1} in 1 M Na_2SO_3 electrolyte.

Chapter 8. General Conclusions

To date, supercapacitor technology has been advancing, with various materials available to replace the high cost RuO_2. Three types of supercapacitors, based on activated carbon, transition metal oxides, and conducting polymers, as well as the innovative solid-state supercapacitors, have attracted most of the attention worldwide in this research field. The main applications of supercapacitors fall into the area of electric and hybrid electric vehicles, providing a large amount of energy stored in small devices. However, there is still a long way to go before supercapacitors are commercialized.

This thesis reports on an investigation into V_2O_5/carbon nanocomposites as supercapacitor electrode materials. These nanocomposite powders were prepared via spray pyrolysis and had an enhanced specific surface area, 18 $m^2 g^{-1}$. The product forms a unique nano-network with nanorods and nanoribbons, agglomerated on spherical shells. In addition, the presence of amorphous carbon increases the conductivity and also contributes to the total capacitance in the terms of pseudocapacitance. The maximum specific capacitance of 295 F g^{-1} was obtained in 2 M KCl electrolyte at a 5-mV s^{-1} scan rate, showing excellent electrochemical performance.

One-dimensional Co_3O_4 nanorods were synthesized through a hydrothermal method, with a further calcination process. Under SEM, the product displayed a morphology of flowerlike agglomerations, which proved to be highly ordered nanoscale rods at high

magnifications. The as-prepared Co_3O_4 nanorods not only exhibited a maximum specific capacitance of 281 F g^{-1} in 2 M KOH solution at a 5-mV s^{-1} scan rate, but also showed excellent cycling stability, with 83.4% retained specific capacitance after 1000 charge-discharge cycles.

Hydrothermal synthesis was utilized to prepare α-Fe_2O_3 nanorods. It is interesting that these small rods (diameters in the range of 20–60 nm) grew in pairs with a pore in the middle. The α-Fe_2O_3 nanorods showed ideal rectangular CV curves with the highest specific capacitance 72 F g^{-1}, obtained in 2 M $Na_2S_2O_3$ solution at a 5-mV s^{-1} scan rate. The electrochemical performance is considered to be affected by the morphology and the specific surface area of this electrode material.

References

[1] S. Trasatti, P. Kurzweil, *Platinum Met. Rev.* 38 (1994) 46.

[2] I. Buchmann (2003), *What's the role of the Supercapacitor?*

Available: http://www.batteryuniversity.com/partone-8.htm.

[3] A. Burke, *J. Power Sources*, 91 (2000) 37–50.

[4] A. Power (2006), *Supercapacitor and Ultracapacitor Applications.*

Available: http://www.axeonpower.com/supercaps.htm.

[5] H.Y. Lee, S.W. Kim, H.Y. Lee, *Electrochem. Commun.* 6 (2004) 499.

[6] S.L. Chou, F.Y. Chen, J. Chen, *J. Power Sources* 162 (2006) 727–734.

[7] K.C. Liu, M.A. Anderson, *J. Electrochem. Soc.* 143 (1996) 124.

[8] C. Lin, J.A. Ritter, B.N. Popov, *J.Electrochem. Soc.* 145 (1998) 4097.

[9] V.R. Shinde, S.B. Mahadik, T.P. Gujar, C.D. Lokhande, *Appl. Surf. Sci.* (2006) (available online).

[10] US patent 2800616, *"Low voltage electrolytic capacitor"*, granted 1957-07-23.

[11] US patent 3288641, *"Electrical energy storage apparatus"*, granted 1966-11-29.

[12] R. Kotz, M.Carlen, *Electrochimica Acta.* 45 (1999) 2483.

[13] M. Winter, R.J. Brodd, *Chem. Rev.* 104 (2004) 4245-4269.

[14] B.E. Conway (1999), *Electrochemical Capacitor, Scientific Fundamentals and Technological Application*, Plenum Press, New York.

[15] C.S. Du, N. Pan, *J. Power Sources*, 160 (2006) 1487–1494.

[16] A. Balducci, R. Dugas, P.L. Taberna, P. Simon, D. Plée, M. Mastragostino, S.

Passerini, *J. Power Sources*, 165 (2007) 922–927.

[17] M. Jayalakshmi, M. Mohan Rao, N. Venugopal, K-B. Kim, *J. Power Sources*, 166 (2007) 578–583.

[18] A.K. Shukla, S. Sampath, K. Vijayamohanan, *Curr. Sci.*, 79 (2000)1656.

[19] P. Sivaraman, V.R. Hande, V.S. Mishra, Ch. Srinivasa Rao, A.B. Samui, *J. Power Sources*, 124 (2003) 351–354.

[20] M. Mastragostino, C. Arbizzani, F. Soavi, *J. Power Sources*, 97-98 (2001) 812-815.

[21] A.L. Beliakov, A.M. Brintsev, Development and application of combined capacitors: double electric layer — pseudocapacity, Proceedings of the 7th International Seminar on Double-layer Capacitors and Similar Energy Storage Devices, Deerfield Beach, FL, December 1997.

[22] I.N. Varakin, A.D. Kiementov, S.V. Litvinenko, N.F. Starodubtsev, A.B. Stepanov, *New ultracapacitors developed by JSC ESMA for various applications*, Proceedings of the 8th International Seminar on Double-layer Capacitors and Similar Energy Storage Devices, Deerfield Beach, FL, December 1998.

[23] Y.M Volfkovich, P.A. Shmatko, *High energy density supercapacitor*, 8th International Seminar on Double-layer Capacitors and Similar Energy Storage Devices, Deerfield Beach, FL, December 1998, paper presented.

[24] K. Naoi, S. Suematsue, A. Manago, *J. Electrochem. Soc.* 147 (2000) 420.

[25] S. Suematsue, K. Naoi, *J. Power Sources*. 97–98 (2001) 816.

[26] K. Naoi, S. Suematsue, M. Hanada, H. Takenouchi, *J. Electrochem. Soc.* 149 (2002) A427.

[27] S. Panero, A. Clemente, E. Spila, *Solid State Ionics* 86-88 (1996) 1285.

[28] A. Clemente, S. Panero, E. Spila, B. Scrosati, *Solid State Ionics* 85 (1996) 273.

[29] C. Arbizzani, M. Mastragostino, M. Meneghello, *Electrochim. Acta* 40 (1995) 2223.

[30] S.A. Hashmi, R.J. Latham, R.G. Linford, W.S. Schlindwein, *Ionics*. 3 (1997) 177.

[31] S.A. Hashmi, R.J. Latham, R.G. Linford, W.S. Schlindwein, *Polym. Int.* 47 (1998) 28.

[32] S.A. Hashmi, H.M. Upadhyaya, *Solid State Ionics* 152–153 (2002) 883.

[33] Z.J. Lao (2006), *Metal Oxides as Electrode Materials for Electrochemical Capacitors*, Master Thesis, University of Wollongong.

[34] C. William (2007), *Materials Science and Engineering: An Introduction*, John Wiley & Sons, Inc., USA.

[35] C.G. Granqvist, *Phys. Scripta* 32 (1985) 401.

[36] I.A. Serbinov, S.M. Babulanam, G.A. Niklasson, C.G. Grangvist, *J. Mater. Sci.* 23 (1988) 2076.

[37] J.B. Goodenough, *J. Solid State Chem.* 3 (1971) 490.

[38] R.M. Wightman, *Science* 204 (1988) 415.

[39] C.G. Granqvist, *Solid State Ionics* 70 (1994) 678.

[40] Y. Fujita, K. Miyazaki, T. Tatsuyama, *Jpn. J. Appl. Phys.* 24 (1985) 1082.

[41] A. Talledo, C.G. Granqvist, *J. Appl. Phys.* 77 (1995) 4655.

[42] J.G. Zhang, J.M. McGraw, J. Turner, D. Ginley, *J. Electrochem. Soc.* 144 (1997) 1630.

[43] C. Julien, B. Yebka, J.P. Guesdon, *Ionics* 1 (1995) 316.

[44] H.Y. Lee, J.B. Goodenough, *J. Solid State Chem.* 148 (1999) 81.

[45] R.N. Reddy, R.G. Reddy, *J. Power Sources* 156 (2006) 700.

[46] Z.J. Lao, K. Konstantinov, Y. Tournaire, S.H. Ng, G.X. Wang, H.K. Liu, *J. Power Sources* 162 (2006) 1451.

[47] K. Konstantinov, J. Wang, S. Bewlay, G. X. Wang, H. K. Liu, S. X. Dou, *J. Metastable and Nanocrystalline Mater.* 15-16 (2003) 325.

[48] Z. W. Zhao, K. Konstantinov, L. Yuan, H. K. Liu, S. X. Dou, *Journal of Nanoscience and Nanotechnology*. 4 (2004) 861.

[49] L. Yuan, K. Konstantinov, G.X. Wang, H.K. Liu, S.X. Dou, *J. Power Sources* 146 (2005) 180.

[50] R.N. Reddy, R.G. Reddy, *J. Power Sources* 124 (1) (2003) 330.

[51] H. Zhang, J.B. Wu, C.X. Zhai, X.Y. Ma, N. Du, J.P. Tu, D.R. Yang, *Nanotechnology*. 19 (2008) 035711.

[52] W.Y. Li, L.N. Xu, J. Chen, *Adv. Funct. Mater.* 851 (2005) 15.

[53] K. T. Nam, D.W. Kim, P. J. Yoo, C.Y. Chiang, N. Meethong, P.T. Hammond, Y.M. Chiang, A.M. Belcher, *Science* 885 (2006) 312.

[54] H-J. Nam, T. Sasaki, N. Koshizaki, *J. Phys. Chem. B* 110 (2006) 23081.

[55] E.M. Logothetis, K. Park, A.H. Meitzler, K.R. Laud, *Appl. Phys. Lett.* 26 (1975) 209.

[56] L. Fu, Z Liu, Y. Liu, B. Han, P. Hu, L. Cao, D. Zhu, *Adv. Mater.* 17 (2005) 217.

[57] J. Jansson, A.E.C. Palmgvist, E. Fridell, M. Skoglundh, L. Osterlund, P. Thormahlen, V. Langer. *J. Catal.* 211 (2002) 387.

[58] P. Thormahlen, M. Skoglundh, E. Fridell, B. Andersson, *J. Catal.* 188 (1999) 300.

[59] J.W.D. Martens, W.L. Peeters, H. M. Van Noort, M. Erman, *J. Phys. Chem. Solids* 46 (1985) 411.

[60] K. Miyatani, K. Kohn, H. Kamimura, S. Iida, *J. Phys. Soc. Jpn.* 21 (1966) 464.

[61] H.K. Kim, T.Y. Seong, J.H. Lim, W.L. Cho, Y.S. Yoon, *J. Power Sources* 167(2001) 102.

[62] L. Cao, M. Lu, H.L. Li, *J. Electrochem. Soc.* 152 (2005) A871.

[63] V.R. Shinde, S.B. Mahadik, T.P. Gujar, C.D. Lokhande, *Appl. Surf. Sci.* 20 (2006) 7487.

[64] Y. Shan, L. Gao, *Mater. Chem. Phys.* 2-3 (2007) 206.

[65] N-L. Wu, S-Y. Wang, C-Y. Han, D-S. Wu, L-R. Shiue, *J. Power Sources.* 113 (2003) 173.

[66] N. Nagarajan, I. Zhitomirsky, *J. Appl. Electrochem.* 36 (2006) 1399.

[67] C. Gong, D. Chen, X. Jiao, Q.Wang, *J. Mater. Chem.* 12 (2002) 1844.

[68] D. Larcher, C. Masquelier, D. Bonnin, Y. Chabre, V. Masson, J.B. Leriche, J.M. Tarascon, *J. Electrochem. Soc.* 150 (2003) A133.

[69] D. Larcher, D. Bonnin, R. Cortes, I. Rivals, L. Personnaz, J.M. Tarascon, *J. Electrochem. Soc.* 150 (2003) A1643.

[70] T. Matsumura, N. Sonoyama, R. Kanno, M. Takano, *Solid State Ionics* 158 (2003) 253.

[71] J. Chen, L.N. Xu,W.Y. Li, X.L. Gou, *Adv. Mater.* 17 (2005) 582.

[72] K.Woo, H.J. Lee, J.P. Ahn, Y.S. Park, *Adv. Mater.* 15 (2003) 1761.

[73] L. Liu, H.Z. Kou, W.L. Mo, H.J. Liu, Y.Q. Wang, *J. Phys. Chem. B.* 110 (2006)

15218.

[74] C.J. Jia, L.D. Sun, Z.G. Yan, L.P. You, F. Luo, X.D. Han, Y.C. Pang, Z. Zhang, C.H. Yan, *Angew. Chem. Int. Ed.* 44 (2005) 4328.

[75] J. Wan, X. Chen, Z. Wang, X. Yang, Y.T. Qian, *J. Cryst. Growth* 276 (2005) 571.

[76] T. Sugimoto, K. Sakata, *J. Colloid Interface Sci.* 152 (1992) 587.

[77] S.H. Sun, H. Zeng, D.B. Robinson, S. Raoux, P.M. Rice, S.X. Wang, G.X. Li, *J. Am. Chem. Soc.* 126 (2004) 273.

[78] H. Deng, X.L. Li, Q. Peng, X. Wang, J.P. Chen, Y.D. Li, *Angew. Chem. Int. Ed.* 44 (2005) 2782.

[79] S. Hamada, E. Matijivic, *J. Colloid Interface Sci.* 84 (1981) 274.

[80] M. Ozaki, S. Kratohvil, E. Matijevic, *J. Colloid Interface Sci.* 102 (1984) 146.

[81] Y.W. Zhu, T. Yu, C.H. Sow, Y.J. Liu, A.T.S.Wee, X.J. Xu, C.T. Lim, J.T.L. Thong, *Appl. Phys. Lett.* 87 (2005) 023103.

[82] R.M. Wang, Y.F. Chen, Y.Y. Fu, H. Zhang, C. Kisielowski, *J. Phys. Chem. B* 109 (2005) 12245.

[83] X.G. Wen, S.H. Wang, Y. Ding, Z.L. Wang, S.H. Yang, *J. Phys. Chem. B* 109 (2005) 215.

[84] K. Byrappa, T. Adschiri, *Prog. Cryst. Growth Char. Mater.* 53 (2007) 117.

[85] S.H. Chen, H. Ma, X.J. Yi, H.C. Wang, et al., *Infrared Phys. Technol.* 45 (2004) 239.

[86] H. Jerominek, F. Picard, D. Vincent, *Opt. Eng.* 32 (1993) 2092.

[87] A.A. Bugayev, M.C. Gupta, *Opt. Lett.* 28 (2003) 1463.

[88] S.H. Chen, H. Ma, X.J. Yi, et al., *Sensor. Actuator. A1* 115 (2004) 28.

[89] T.D. Manning, I.P. Parkin, M.E. Pemble, et al., *Chem. Mater.* 16 (2004) 744.

[90] F.J. Morin, *Phys. Rev. Lett.* 34 (1959) 34.

[91] D.H. Youn, J.W. Lee, B.G. Chae, H.T. Kim, S.L. Maeng and K.Y. Kang, *J. Appl. Phys.* 95 (2004) 1407.

[92] G. Guzman, R. Morineau and J. Livage, *Mater. Res. Bull.* 29 (1994) 509.

[93] S. Pavasupree, Y. Suzuki, A. Kitiyanan, *J. Solid State Chem.* 178 (2005) 2152.

[94] X.Y. Chen, X. Wang, Z.H. Wang, J.X. Wan, J.W. Liu and Y.T. Qian, *Nanotechnology* 15 (2004) 1685.

[95] C.K.C. Kam and A.K. Cheetham, *Mater. Res. Bull.* 41 (2006) 1015.

[96] F. Sediri, F. Touati and N. Gharbi, *Mater. Sci. Eng. B* 129 (2006) 251.

[97] F. Sediri and N. Gharbi, Mater. *Sci. Eng. B* 139 (2007) 114.

[98] D.C. Harris (2003), *Quantitative Chemical Analysis, 6th ed.* W.H. Freeman, New York.

Definitions

The following definitions, referred to Refs. [13] and [98], are used during the course of discussions on batteries, fuel cells, and electrochemical capacitors.

A *battery* is one or more electrically connected electrochemical cells having terminals/contacts to supply electrical energy.

The *anode* is the negative electrode of a cell associated with oxidative chemical reactions that release electrons into the external circuit.

The *cathode* is the positive electrode of a cell associated with reductive chemical reactions that gain electrons from the external circuit.

A *separator* is a physical barrier between the positive and negative electrodes incorporated into most cell designs to prevent electrical shorting. The separator can be a gelled electrolyte or a microporous plastic film or other porous inert material filled with electrolyte. Separators must be permeable to the ions and inert in the battery environment.

A *fuel cell* is an electrochemical conversion device that has a continuous supply of fuel such as hydrogen, natural gas, or methanol and an oxidant such as oxygen, air, or

hydrogen peroxide. It can have auxiliary parts to feed the device with reactants as well as a battery to supply energy for start-up.

An *electrochemical capacitor* is a device that stores electrical energy in the electrical double layer that forms at the interface between an electrolytic solution and an electronic conductor. The term applies to charged carbon-carbon systems as well as carbon battery electrode and conducting polymer electrode combinations, sometimes called ultracapacitors, supercapacitors, or hybrid capacitors.

Discharge is an operation in which a battery delivers electrical energy to an external load.

Charge is an operation in which the battery is restored to its original charged condition by reversal of the current flow.

Working electrode is an electrode at which the reaction of interest occurs.

Reference electrode is an electrode that maintains a constant potential against which the potential of another half-cell may be measured.

Counter electrode is the current-carrying partner of the working electrode. Same as auxiliary electrode.

List of Abbreviations

XRD	X-ray diffraction
SEM	Scanning Electron Microscope
TEM	Transmission Electron Microscope
BET	Brunauer-Emmett-Teller gas sorption technique
TGA	Thermogravimetric Analysis
CV	Cyclic Voltammetry
SCE	Saturated Calomel Electrode (reference electrode)
wt%	Weight percent